Published in final edited form as:
Nat Metab. 2019 November ; 1(11): 1127–1140. doi:10.1038/s42255-019-0137-5.

Autophagic lipid metabolism sustains mTORC1 activity in TSC-deficient neural stem cells

Chenran Wang[*], **Michael A. Haas**, **Fuchun Yang**, **Syn Yeo**, **Takako Okamoto**, **Song Chen**, **Jian Wen**[#], **Pranjal Sarma**, **David R. Plas**, **Jun-Lin Guan**[*,&]
Department of Cancer Biology, University of Cincinnati College of Medicine, Cincinnati, OH 45267

Abstract

Although mTORC1 negatively regulates autophagy in cultured cells, how autophagy impacts mTORC1 signaling, in particular in vivo, is less clear. Here we show that autophagy supports mTORC1 hyperactivation in NSCs lacking Tsc1, thereby promoting defects in NSC maintenance, differentiation, tumourigenesis, and the formation of the neurodevelopmental lesion of Tuberous Sclerosis Complex (TSC). Analysing mice that lack Tsc1 and the essential autophagy gene Fip200 in NSCs we find that TSC-deficient cells require autophagy to maintain mTORC1 hyperactivation under energy stress conditions, likely to provide lipids via lipophagy to serve as an alternative energy source for OXPHOS. In vivo, inhibition of lipophagy or its downstream catabolic pathway reverses defective phenotypes caused by Tsc1-null NSCs and reduces tumorigenesis in mouse models. These results reveal a cooperative function of selective autophagy in coupling energy availability with TSC pathogenesis and suggest a potential new therapeutic strategy to treat TSC patients.

Keywords

mTORC1; autophagy; lipid catabolism; energy stress; neural stem cells; tumorigenesis

Introduction

Mechanistic target of rapamycin complex 1 (mTORC1) is a master regulator of cellular homeostasis for growth, proliferation, differentiation, metabolism, and survival[1–3].

---

[*] Corresponding authors Correspondence and materials requests: Chenran Wang, Jun-Lin Guan. ([&]contact author) Phone: 513-558-5323, Fax: 513-558-5061, guanjl@uc.edu.

[#] Present address: Department of Breast Surgery, the Fourth Affiliated Hospital of China Medical University, Shenyang, Liaoning, China 110032.

Contributions

CW, JLG: project concept, research design, data analysis, manuscript writing. CW: experiments. CW and: MAH: mouse model analyses, OCR assay; JW: immunoblots; PS, DRP: fatty acid beta-oxidation assay; SY: FACS analysis. FY, TO: generated Atg7 KO in WT and Tsc2 KO MEF. SC: constructed Atg5 KO in Rheb-CA MEF.

Competing interest statement

The authors declare no conflict of interests for this manuscript.

Data availability

The data that support the findings of this study are available from the corresponding author upon request. Gel source data are shown in Source data Figure 1-Figure 5.

mTORC1 is hyperactivated in the autosomal dominant disorder tuberous sclerosis complex (TSC) and is associated with developmental defects and increased tumorigenesis, especially in brain. Neurological symptoms of TSC cause significant disability and morbidity[4, 5]. Subependymal nodule (SEN) and benign subependymal giant astrocytoma (SEGA) tumors are characteristic of TSC[6]. SEN/SEGA expressing neural stem/progenitor cell (NSC) markers localize within the subventricular zone (SVZ), a postnatal neurogenesis region in humans and rodents, suggesting abnormal NSC proliferation and transformation. Indeed, recent studies showed that deletion of *Tsc1* or *Tsc2* in mouse NSCs led to NSCs depletion, aberrant migration and differentiation, murine SEN-like lesion formation, and other Tsc-associated brain defects in several different mouse models[7–10]. Developing treatment strategies for TSC requires understanding mTORC1 control of NSC proliferation and differentiation.

Recent studies suggest the importance of metabolism in the regulation of NSC homeostasis, quiescence, and differentiation[11–13]. Interestingly, postnatal NSCs use free fatty acid (FFA) oxidization for energy[14, 15]. In Tsc-deficient cells, metabolism is rewired by mTORC1 hyperactivation, leading to increased aerobic glycolysis[16, 17], fatty acid (FA) synthesis via SREBP and S6K1 signaling[18, 19], and nucleotide synthesis[20].

Autophagy is a conserved process that sequesters and delivers cytoplasmic materials to lysosomes for degradation and recycling[21–23]. Hyperactivation of mTORC1 in Tsc-deficient cells suppresses autophagy[24], but we recently found increased autophagy in glucose-starved Tsc1-deficient breast cancer cells [25]. Others have reported increased autophagy in Tsc-deficient neurons and cortical tubers from TSC patients[26]. Autophagy promotes progression of Tsc2KO xenograft tumors and Tsc2 +/−mouse spontaneous renal tumors[27]. Dysfunctions in selective autophagy, ie, aggrephagy (depleting protein aggregates)[28] and mitophagy (degrading mitochondria)[29, 30], have been linked to neurodegeneration[31]. Lipophagy (sequestering lipid droplets [LDs] by autophagosomes)[32, 33] in neurons modulated the thermal response of peripheral tissue under cold stress[34], suggesting novel autophagy functions besides anti-neurodegenerative roles[35, 36]. Our recent studies showed that autophagy of p62 aggregates is required for postnatal NSC self-renewal and function[37, 38], but little is known about the role of autophagy-mediated regulation of mTORC1 in NSCs in vivo.

We generated a novel Tsc1 and FIP200 (FAK interacting protein of 200 KD) double conditional knockout mouse model to test mTORC1 regulation by autophagy in vivo. Results showed that inactivation of FIP200-mediated autophagy reversed mTORC1 hyperactivation in Tsc1-null NSC, rescuing defective maintenance and differentiation and reducing murine SEN-like lesion formation. FIP200 ablation reduced autophagy release of FFAs from LDs for β-oxidation, OXPHOS, and ATP production under energy stress conditions. Targeting autophagy and its downstream lipolysis pathway decreased mTORC1 hyperactivation and reversed pathological defects in Tsc1-deficient NSCs in vivo.

Results

FIP200 ablation in $Tsc1^{GFAP}$ cKO mice reverses brain abnormalities driven by mTORC1 hyperactivation

Recent studies showed that mTORC1 hyperactivation[7] and autophagy deficiency[37, 38] both led to defective maintenance of neural stem/progenitor cells (NSCs). Autophagy inhibition by mTORC1 hyperactivation is well established[1, 3, 39], but it is not known if reduced autophagy is responsible for NSCs defects[7–9]. To explore this question, we generated $Tsc1^{f/f}$;$Fip200^{f/f}$;*hGFAP-Cre* (designated as 2cKO), $Tsc1^{f/f}$;$Fip200^{f/+}$;*hGFAP-Cre* ($Tsc1^{GFAP}$cKO), and $Tsc1^{f/+}$;$Fip200^{f/+}$;*hGFAP-Cre* (Ctrl) mice by crossing $Tsc1^{f/f}$[40, 41] and $Fip200^{f/f}$;*hGFAP-Cre*[38] mice. Mice were produced in expected Mendelian ratios. Despite NSC defects by either *Tsc1* or *Fip200* deletion alone, we found that, surprisingly, the 2cKO mice were rescued from aberrant growth in the subventricular zone (SVZ) and rostral migratory stream (RMS), and enlarged brains compared to $Tsc1^{GFAP}$cKO mice[7, 9] (Figs. 1A, 1B, ED1A, ED1B). Autophagy was functional in $Tsc1^{GFAP}$cKO but reduced in 2cKO SVZ, indicated by p62 aggregates and autophagy flux, consistent with autophagy blockade with FIP200 loss[37, 38, 42] (Figs. 1C, 1D, Fig. ED1C-1F). Staining of phosphorylated S6 ribosomal protein (pS6RP) and 4EBP1 (p4EBP1), downstream effectors of mTORC1, revealed diminished mTORC1 activity in the SVZ of 2cKO mice (Figs. 1E, 1F, ED1G, ED1H). These results suggested that abnormal $Tsc1^{GFAP}$cKO NSCs were associated with sustained autophagy combined with mTORC1 hyperactivation.

Autophagy inhibition in $Tsc1^{GFAP}$ cKO mice rescues Tsc1-deficient NSCs and suppresses tumorigenesis

We next examined the cellular basis for the rescue of brain defects in 2cKO mice. At P0, Ki67$^+$ cell frequency was increased in the VZ/SVZ of $Tsc1^{GFAP}$cKO mice compared to Ctrl (Fig. 1G), contributing to increased cellularity and RMS cell migration at P7 and P21 (see Figs. 1A, 1B)[7, 9]. In $Tsc1^{GFAP}$ cKO mice at P21, Ki67$^+$ cell frequency was reduced and apoptosis increased compared to Ctrl (Figs. 1H, 1I). Fip200 deletion in 2cKO mice restored VZ/SVZ proliferation and apoptosis, and NSC proliferation, to Ctrl levels (Figs. 1G–1K, ED1I-1J).

We examined NSC self-renewal by in vitro neurosphere assay using P21 SVZ cells. Primary neurospheres from $Tsc1^{GFAP}$cKO and 2cKO SVZ cells were similar in number and size to those from Ctrl (Figs. 1L, ED1K, ED1L). $Tsc1^{GFAP}$cKO secondary neurosphere growth was significantly decreased compared to Ctrl and 2cKO (Figs. 1L, 1M, ED1M), suggesting that Fip200 deletion sustained the renewal potential of Tsc1-deficient NSCs. Autophagy in $Tsc1^{GFAP}$cKO and Ctrl neurospheres was similar, and was blocked in 2cKO neurospheres by Fip200 deletion (Figs. ED1N, ED1O). As previously observed[7, 9], increased DCX$^+$ neuroblasts were found in $Tsc1^{GFAP}$cKO mice at P21 (Figs. 1N, ED2A). Mature neurons (NeuN$^+$ cells) were found in $Tsc1^{GFAP}$cKO SVZ (Fig. 1O). Labeling proliferative SVZ cells with BrdU at P7 and tracing to P21, we found ~7% NeuN$^+$BrdU$^+$ cells in $Tsc1^{GFAP}$cKO SVZ but almost none in Ctrl SVZ (Figs. 1P, 1Q)[37, 38]. This indicates premature differentiation of mutant neuroblasts consistent with either defective migration into RMS or prevention of migration out of the SVZ. *Fip200* deletion reversed aberrantly increased DCX

$^{+}$ neuroblasts, NeuN^{+} cells, NeuN^{+}BrdU^{+} cells, and astrocytes in 2cKO SVZ (Figs. 1N–1R, ED2B). Culturing neurospheres in vitro[38] to analyze *Tsc1*^{GFAP}cKO SVZ cell differentiation, we found aberrantly increased β-III tubulin^{+} cells (Fig. ED2C), GFAP^{+} astrocytes (Fig. ED2D), and reduced NeuN+ neurons (Fig. ED2E) and MBP+ cells (Fig. ED2F); all were rescued in 2cKO neurospheres, consistent with observations in vivo. These results suggest that autophagy is required for the defective maintenance and differentiation of Tsc1-deficient NSCs induced by hyperactivation of mTORC1 in *Tsc1*^{GFAP}cKO mice.

SEN/SEGAs are brain lesions found in TSC patients. SEN-like lesions in the SVZ of *Tsc1*^{GFAP}cKO mice (Fig. ED2G) were not found until P21. They developed along the lateral wall on the side of striatum with no regional preference (Figs. 1S, 1T). Some lesions appeared as “floating” spheres as tumors protruded and bent in the LV when cross-sectioned (Fig. 1S, arrow). Murine SEN-like cells contained hyperchromatic nuclei surrounded by scanty cytoplasm, resembling NSC, and were pS6RP^{+} (Fig. ED2H). As previously reported[43], proliferation in the SEN-like lesions was lower than in SVZ (~5% vs ~20% Ki67^{+} cells at P21). SEN-like cells were nestin^{+} (Fig. ED2I); most were medium Sox2^{+} compared to strong Sox2^{+} in *Tsc1*^{GFAP}cKO mice (Fig. ED2J); some were NG2^{+} (Fig. ED2K); and most expressed high levels of DCX (Fig. ED2L). Only a small fraction was GFAP^{+} (Fig. ED2J), suggesting mixed lineage with neuronal differentiation preference. We found only one SEN-like lesion in ten 2cKO mice at P21 and none out of six at P28 (Fig. 1T, ED2G). These results suggest that autophagy supports tumorigenesis with hyperactivated mTORC1 in *Tsc1*^{GFAP}cKO mice.

Many autophagy genes have functions independent of their roles in canonical autophagy. We studied autophagy-specific functions of FIP200 in vivo using our Fip200 4A knock-in mutant mouse, in which the autophagy function of FIP200 is inactivated[44]. Removing the FIP200 autophagy function in *Tsc1*$^{f/f}$*;Fip200*$^{f/KI}$;*hGFAP-Cre* (designated 2cKI) mice in Tsc1-deficient NSC rescued elevated SVZ cell number, mTORC1 hyperactivation, defective NSC maintenance (Fig. ED2M-ED2R), and SEN-like lesion formation (Fig. 1T), similar to FIP200 ablation. These results support that autophagy is required for defective NSC maintenance, differentiation, and tumorigenesis in *Tsc1*^{GFAP}cKO mice.

Energy-stressed Tsc-deficient cells require autophagy for hyperactivation of mTORC1

To explore the mechanisms by which autophagy inhibition reverses NSC defects and tumorigenesis in *Tsc1*^{GFAP}cKO mice, we first examined mTORC1 activation in Tsc2 KO MEF cultured under various conditions. The accumulation of LC3-II and LC3 puncta in response to Bafilomycin A1 (BafA1) was comparable in Tsc2 KO and WT MEF under basal and glucose-free conditions (Figs. ED3A, ED3B). Both glucose and amino acid starvation reduced mTORC1 phosphorylation of S6K in WT, while Tsc2 KO MEF had sustained mTORC1 signaling (Fig. ED3C). Inhibition of autophagy by Spautin1[45] significantly reduced mTORC1 hyperactivation in glucose starved but not amino acid starved Tsc2 KO MEF (comparing lanes 7 and 8; 11 and 12). mTORC1 is activated on lysosomes[46], and mTOR was found on LAMP2^{+} (Lysosomal Associated Membrane Protein 2) lysosomes in Tsc2 KO MEF under glucose-free conditions. Spautin1 treatment abolished co-localization (Figs. ED3D, ED3E). Spautin1 autophagosome inhibition was verified by measuring LC3-II with or without BafA1 treatments (Fig. ED3F). To complement pharmacological inhibition of autophagy, we generated Atg7 KO in WT and Tsc2 KO MEF (Fig. ED3G). This genetic block of autophagy decreased hyperactivation of mTORC1 and abolished co-localization of mTOR and LAMP2 in glucose-free conditions (Figs. ED3G, ED3H, see Fig. ED3D bottom panels and Fig. ED3E). Consistent with Tsc-deficient MEF, mTORC1 hyperactivation in *Tsc1*^{GFAP}cKO neurospheres was reversed in 2cKO to Ctrl levels under glucose-free conditions (Figs. 2A, 2B). These results correspond to mTORC1 activation status in SVZ (see Figs. 1E, 1F), connecting in vitro mechanistic studies using MEF/SVZ cells and observations in vivo.

Interrupting autophagy by Spautin1 treatment or Atg7 KO induced AMPK phosphorylation of its targets Raptor at Ser^{792} and ACC at Ser^{79} in Tsc2 KO MEF in response to glucose starvation or glycolysis inhibitor 2-deoxy-d-glucose (2DG) (Figs. ED4A, S4B). Autophagy inhibition by either Spautin1, chloroquine (CQ), or Atg7 KO decreased ATP content (Figs. ED4C, ED4D), accounting for increased AMPK activity. In vivo, an increased fraction of pACC+ and pAMPK+ cells in SVZ of 2cKO compared to *Tsc1*^{GFAP}cKO mice was seen (Figs. 2C–2F). Likewise, ATP was increased in *Tsc1*^{GFAP}cKO neurospheres, and reversed in 2cKO neurospheres (Fig. 2G). Glucose-free conditions in SVZ cells and MEF may approximate the relatively low glucose concentration in SVZ[47].

We stably expressed scrambled (Ctrl), TSC1, or FIP200 shRNA singly or in combination (Figs. ED4E-ED4G) in HEK293 cells. Lack of increase in LC3-II with BafA1 indicated decreased autophagy after FIP200 knockdown (Figs. ED4H-ED4I). FIP200 knockdown decreased hyperactivation of mTORC1 induced by TSC1 knockdown in cells treated with 2DG (Fig. ED4J), but not normal culture conditions (see Fig. ED4E). These results suggested that FIP200-mediated autophagy is necessary to maintain mTORC1 hyperactivation with loss of either Tsc1 or Tsc2 under energy stress conditions.

Autophagy maintains OXPHOS to sustain ATP production for hyperactivated mTORC1

Autophagy is proposed to provide substrates for oxidative metabolism under energy stress[48, 49]. We studied mitochondrial oxygen consumption rate (OCR) and found that Tsc2 KO MEF had increased ATP-related and maximum OCR (Figs. 2H, ED4K, ED4L), indicative of high mitochondrial oxidative phosphorylation (OXPHOS). After glucose deprivation (Fig. ED4K) or 2DG treatment (Fig. ED4L), both OCRs were significantly reduced in WT but maintained in Tsc2 KO MEF. Autophagy inhibition by Spautin1, CQ, or Atg7 KO reduced OCRs in Tsc2 KO MEF (Figs. 2I, 2J, ED4M, ED4N), consistent with reduced ATP (see Figs. ED4C, ED4D). Similarly, Tsc1 KD cells (Figs. 2K, 2M) and WT MEF expressing constitutively active Rheb (Rheb-CA MEF) (Fig. 2L, 2N) maintained OCR in glucose-free conditions in an autophagy-dependent manner. Lastly, increased ATP-related and maximum OCR in *Tsc1*^{GFAP}cKO neurospheres were reversed in 2cKO (Fig. 2O). Together, these results suggest a role of autophagy in maintaining elevated OXPHOS to sustain ATP production and mTORC1 hyperactivation under energy stress.

Lipophagy produces FFAs as an energy source for hyperactivation of mTORC1

We explored potential autophagy-dependent energy sources to fuel mTORC1 activity in energy stressed Tsc-deficient cells. Glutamine did not restore mTORC1 hyperactivation in Tsc2 KO MEF after autophagy inhibition (Fig. ED5A), in contrast to previous results in pancreatic cancers [50]. Amino acid carbon skeletons were unlikely energy sources, as similar ammonia concentrations were found in WT and Tsc2 KO MEF under normal or glucose-free conditions (Fig. ED5B). Glycogen content was comparable in WT and Tsc2 KO MEF after glucose starvation (Fig. ED5C), and BafA1 had no effect, suggesting autophagy did not regulate glycogen levels (Fig. ED5C).

We then focused on lipid catabolism. Previous studies showed that Tsc-deficient cells have higher triglyceride (TG) stores than WT cells[51]. Glucose deprivation significantly promoted glycerol release in Tsc2 KO but not WT MEF (Fig. 3A); Spautin1 reduced it. Glucose deprivation and 2DG decreased TG and increased intracellular FFAs in Tsc2 KO MEF; Spautin1 treatment counteracted these changes (Figs. 3B, 3C). FFAs were increased in TSC1-knockdown after glucose starvation, but not normal culture conditions, and this increase was abolished by autophagy inhibition by FIP200 knockdown (Fig. ED5D). In mammalian cells, TG is stored in organelles as lipid droplets (LDs). The baseline number of LDs in Tsc2 KO was higher than WT MEF. Glucose deprivation reduced LDs in Tsc2 KO but not WT MEF in an autophagy-dependent manner (Figs. 3D, 3E). $Tsc1^{GFAP}$cKO neurospheres maintained increased LDs; glucose deprivation significantly reduced LDs in $Tsc1^{GFAP}$cKO but not in 2cKO neurospheres (Figs. 3F, 3G).

LDs can be sequestered by autophagosomes and transported to lysosomes for degradation by lipophagy[32]. Under glucose-free conditions LDs co-localized with $LC3^+$ autophagosomes in $Tsc1^{GFAP}$cKO but not Ctrl or 2cKO neurospheres (Figs. 3H, 3I). Co-localization of LC3 and LDs was slightly induced upon glucose starvation in both WT and Tsc2-deficient MEF; the co-localization of LDs with autophagosomes was significantly increased by BafA1 (Figs. 3J, ED5E) and abolished by Spautin1. Similar results were obtained for co-localization of LDs with lysosomes (Figs. 3K, ED5F). In vivo, we observed fewer LDs in $Tsc1^{GFAP}$cKO versus Ctrl SVZ (Fig. ED5H-ED5M), consistent with higher fatty acid oxidation. Both the mitochondrial β-oxidation inhibitor etomoxir (ETO) and genetic autophagy inhibition (2cKO) increased LDs, suggesting that the lipid content of SVZ cells is responsive to mitochondrial beta-oxidation, which requires functional autophagy (Fig ED5M). These results indicate that lipophagy facilitates FFA production from stored TGs as an energy source for TSC deficient cells under energy stress to maintain mTORC1 hyperactivation.

β-oxidation of FFAs supports bioenergetics in Tsc-deficient cells during energy stress

FFAs can be metabolized to produce ATP through catabolic β-oxidation. We analyzed β-oxidation under glucose-free conditions and found higher activity in Tsc2 KO MEF, reversed by Spautin 1 treatment (Fig. 3L). We then cultured Tsc2 KO MEF with medium and long chain FFA. After autophagy inhibition, we found that both FFAs abrogated ATP loss by Spautin1 and CQ under glucose-free (Fig. 3M) but not normal culture conditions (Fig. ED5G). Consistent with ATP, under energy stress long chain FFAs increased the OCR (Fig. 3N) and restored S6RP phosphorylation (Fig. 3O) in Spautin1-treated Tsc2 KO but not WT

MEF. These results demonstrate a role for autophagy-mediated lipid catabolism in Tsc-deficient cells under energy stress conditions.

We then examined FFA β-oxidation directly and found that treatment with β-oxidation inhibitors ETO, trimetazidine (TMZ)[52], and ranolazine (Rano)[53] triggered bioenergetic stress characterized by phosphorylation of AMPK, Raptor, and ACC (Figs.4A, ED6A, ED6C), and reduced phosphorylation of ED6K and ED6RP (Figs. 4B, ED6B, ED6D) in Tsc2 KO MEF under glucose-free and 2DG treatment. ETO inhibited mTORC1 activation under energy stress but not normal culture in *Tsc1*^{GFAP}cKO neurospheres (Fig. 4C). ETO and Rano dissociated mTOR from LAMP2+ structures in Tsc2 KO MEF under glucose deprivation (Figs. ED6E, bottom panels and ED6F, compare to Fig. ED3D, second row right 3 panels and S3E), but not normal culture conditions (Figs. ED6E, top panels, ED6F). Lastly, inhibition of AMPK by Compound C prevented mTORC1 suppression by ETO (Fig. ED6G) in Tsc2 KO MEF, providing further support that FAO inhibitors blocked mTORC1 via AMPK in TSC-deficient cells under energy stress.

All β-oxidation inhibitors reduced ATP levels in Tsc2 KO (Fig. 4D) but not WT (Fig. ED6H) MEF under energy stress. Similar results were obtained for TSC1 KD cells treated with ETO (Fig. ED6I). ETO and Rano also decreased ATP levels under energy stress in *Tsc1*^{GFAP}cKO neurospheres (Fig. 4E). We also observed corresponding decrease of maximum OCR in Tsc2 KO MEF by all inhibitors under energy stress (Figs. 4F, 4G). These results suggest that Tsc-deficient cells have an increased dependence on FFA β-oxidation fueled by FFAs to maintain hyperactivated mTORC1 under energy stress.

All three β-oxidation inhibitors also increased the number of LDs co-localized with lysosomes in Tsc2 KO but not in WT MEF under glucose deprivation (Figs. 4H, 4I). Co-localization of LDs with LC3+ autophagosomes increased together with FFAs (Fig. 4J, 4K), suggesting feedback to increase lipophagy when β-oxidation is inhibited. These results further support that FFAs generated by lipophagy of LDs are used to sustain mTORC1 hyperactivation in Tsc-deficient cells under energy stress.

Lysosome acid lipase (LAL) digests LDs to release FFAs in Tsc-deficient cells

We next explored potential lipase(s) for lipophagy of LDs. We used lipase inhibitors including Orlistat for lysosomal acidic lipase (LAL)[54], Atglistat for adipose triglyceride lipase (ATGL)[55], and JZL184 for monoacylglycerol lipase[56]. Similar to a previous report suggesting a role for LAL in autophagy[57], we found that Orlistat, but not Atglistat or JZL184, significantly reduced glycerol release (Fig. 5A) and increased the number of LDs (Fig. 5B) in Tsc2 KO MEF with glucose starvation. No inhibitor affected glycerol release in normal culture conditions, nor did they affect glycerol release or LD numbers of WT MEF under either condition (Figs. ED7A, ED7B). Orlistat also blocked FFA release (Fig. 5C), reduced mitochondrial OCR (Fig. 5D), and suppressed ATP content (Fig. 5E) of Tsc2 KO MEF under both glucose-free and 2DG treatment conditions. Consequently, Orlistat increased the AMPK phosphorylation of Raptor at Ser^{792} and ACC at Ser^{79}, reduced mTORC1-dependent phosphorylation of S6K and S6RP (Figs. 5F, 5G), and disrupted co-localization of mTOR with LAMP2 in Tsc2-deficient cells under glucose-free conditions (Fig. ED7C). Importantly and consistent with results in Tsc-deficient MEF, we found that

Orlistat reduced mTORC1 activation under energy stress, but not normal culture conditions in *Tsc1*^{GFAP}cKO primary SVZ neurospheres (Fig. 5H). Lastly, blockade of LAL resulted in increased localization of LDs on lysosomes (marked by LAMP2) in Tsc2 KO MEF under glucose starvation condition (Fig. 5I). As LAL is the only lipase known to degrade lipids in lysosomes[58], these results suggest that under energy stress conditions, LDs are delivered to lysosomes via lipophagy, and LAL is used to hydrolyze TG to generate FFAs to sustain ATP and mTORC1 hyperactivation in Tsc-deficient cells.

Indeed, we observed increased LAL in Tsc2 KO MEF (Fig. ED7D). In glucose-starved Tsc2 KO MEF, expression of LAL shRNA (Fig. ED7E) reduced glycerol release (Fig.ED7F) and FFA content (Fig. ED7G), accompanied by corresponding increases in LDs (Fig. ED7H) and TG (Fig. ED7I). LAL shRNA also decreased mitochondrial OCR, ATP levels, and mTORC1 activation under energy stress (Figs. ED7J-ED7L). Supplementation of BSA-Palmitate restored ATP and mTORC1 hyperactivation in Tsc2 KO MEF lacking LAL in glucose limiting conditions (Fig. 5J, ED7K). Together, these results demonstrate LAL as the major lipase for the production of FFAs from lipophagy of LDs to sustain hyperactivated mTORC1 in Tsc deficient cells under energy stress.

Lipophagy inhibition restores function of Tsc1-deficient NSCs and inhibits tumorigenesis

To evaluate targeting lipophagy to counteract mTORC1 hyperactivation as new therapies, we examined pharmacological inhibition of autophagy in *Tsc1*^{GFAP}cKO mice. We injected autophagy inhibitor CQ (50 mg/kg) and glycolysis inhibitor 2DG (500 mg/kg) I.P. into P7 Ctrl and *Tsc1*^{GFAP}cKO mice every other day for 14 days, individually or in combination. Combined CQ+2DG inhibited murine SEN-like lesions, but each alone did not (Fig. 6A). Lesions were also eliminated by positive control rapamycin (2.5 mg/kg, daily I.P.). Combined CQ+2DG, but neither alone decreased S6RP phosphorylation (Figs. 6B, ED7M) and increased AMPK phosphorylation and ACC (Figs. 6C, 6D, ED7N, ED7O). mTORC2 was unaffected (Figs. ED7P, ED7Q). 2DG, CQ, or the combination all reduced ERK signaling comparably (Figs. ED7R, ED7S). The combination treatment restored the pool of GFAP^{+}Nestin^{+} and GFAP^{+}Sox2^{+} NSC (Figs. 6E, ED8A). Combination CQ+2DG decreased proliferation and apoptosis (Figs. 6F, 6G, ED8B), aberrant neurogenesis and premature neuronal differentiation, and increased astrogenesis (Figs. 6H–6J) of *Tsc1*^{GFAP}cKO but single treatment had no effect on mTORC1 activity, or the maintenance and differentiation of SVZ NSC in Ctrl mice (Figs. 6B–6J).

We next tested β-oxidation inhibitors ETO, Rano, and TMZ with or without 2DG in mice. The combination blocked tumorigenesis, but β-oxidation inhibitors alone did not (see Fig. 6A). Phosphorylation of AMPK and ACC increased (Figs. 6K–6L), and mTORC1 signaling was reduced (Fig. 6M) in *Tsc1*^{GFAP}cKO but not Ctrl mice. The combination rescued defective NSC maintenance, proliferation, and apoptosis (Figs.6N-6P, ED8C, ED8D), and neurogenesis and neuronal differentiation defects (Figs. ED8E, ED8F) in *Tsc1*^{GFAP}cKO but not Ctrl mice. β-oxidation inhibitors alone did not alter AMPK and ACC phosphorylation, mTORC1 activation, or proliferation and apoptosis in *Tsc1*^{GFAP}cKO mice (Figs. 6K–6P). Each suppressed aberrant neurogenesis and neuronal differentiation (Figs. ED8E, ED8F) without affecting SEN-like lesion formation (see Fig. 6A) in *Tsc1*^{GFAP}cKO mice. Together, these results indicate that combined inhibition of glycolysis and lipophagy, or their downstream catabolic processes, prevents tumorigenesis, exhaustion, and abnormal NSC differentiation, establishing the therapeutic potential of autophagy inhibition for Tsc-deficient conditions.

Discussion

In mice with *Fip200* and *Tsc1* deletion we surprisingly found that autophagy deficiency rescued defective NSCs caused by mTORC1 hyperactivation. The working model (Fig. 6Q) outlines a new paradigm of mTORC1 regulation by selective lipophagy and lipid catabolism required to fuel mTORC1 hyperactivation in Tsc-deficient NSCs. mTORC1 hyperactivation in Tsc-deficient cells increases aerobic glycolysis, FA synthesis, and lipid storage[16, 51]. In SVZ tissue in vivo and various cells under energy stress in vitro, autophagy was sustained despite Tsc-deficiency to meet increased energy demands. mTORC1 hyperactivation increases protein synthesis[59] and must be coordinated with cellular energy status[60]. Under nutrient-rich conditions, increased glycolytic activity and OXPHOS[61] provide energy. In the absence of glycolysis, lipophagy mechanisms described here could support elevated protein synthesis and energy expenditure. Nevertheless, we recognize that the absence of tracing experiments for metabolites to provide direct evidence for each intermediate of the working model (see Fig. 6Q) is a limitation of the study. Despite this, both genetic and pharmacological approaches in animal and cell models clearly established a role for lipophagy to meet energy demands in Tsc1-null NSC. These results add FAs to a growing list of metabolic outputs from autophagy upstream of mTORC1.

FIP200 single knockout mice are depleted of NSCs[38], but FIP200 knockout in the Tsc1-deficient background rescued NSC maintenance (this study), further highlighting the metabolic re-wiring by mTORC1 hyper-activation in NSCs. Previously, we proposed that FIP200 regulates normal NSCs via its functions distinct from canonical autophagy that is dependent on Atg5, Atg7 or Atg16L1 [37]. In Tsc-deficiency with energy limitation, however, the autophagy function of FIP200 becomes required for neoplastic phenotypes driven by mTORC1 hyper-activation. Importantly, blocking only FIP200 autophagy function, like ablation of the FIP200 gene, rescued NSC phenotypes in 2cKI mice.

Autophagy inhibition by gene ablation has been shown to decrease tumorigenesis and progression in several mouse models of cancer, including breast, lung and pancreatic cancer[62–64]. Our studies advance autophagy inhibition for cancer therapy, and establish new links between autophagy, lipid catabolism, and bioenergetics. In vivo inhibition of tumorigenesis by targeting either lipophagy or lipid catabolism suggests new therapeutic strategies for TSC and other diseases with mTORC1 hyperactivation.

Methods

Animals

FIP200$^{f/f}$, *FIP200*$^{f/KI}$, *Tsc1*$^{f/f}$and *hGFAP-Cre* transgenic mice were described previously[37, 38, 41, 44]. *FIP200*$^{f/f}$;*Tsc1*$^{f/f}$*;hGFAP-Cr*e, *FIP200*$^{f/KI}$;*Tsc1*$^{f/f}$*;hGFAP-Cr*e and control mice were maintained on a mixed C57Bl6 (87.5%) with FVB (12.5%) background.

Age and littermate-matched control and mutant mice were used for analysis to minimize the impact of modifier genes. Mice were housed and handled according to local, state, and federal regulations. All experimental procedures were carried out according to the guidelines of Institutional Animal Care and Use Committee at the University of Cincinnati. Genotyping for *FIP200*, *Tsc1* and Cre alleles was performed by PCR analysis of tail DNA essentially as described previously[41].

Cells and cell culture

Human embryonic kidney 293 cells (HEK293) from ATCC is cultured in DMEM with 10% FBS under growth conditions. Human Tsc1, FIP200 shRNA, and scrambled shRNA infected HEK293 cells were selected with 1 μg/ml Puromycin in media. Wild type (WT) mouse embryonic fibroblast (MEF) and Tsc2 knockout MEF were kindly gifted by Dr. Diane Fingar from the Department of Cell and Developmental Biology, University of Michigan and cultured in DMEM with 10% FBS and 25 μg/ml Hygromycin B for selection. Atg5 knockout MEF and paired WT MEF were gifted by Dr. Noboru Mizushima from the University of Tokyo. Atg5 KO MEF and WT MEF were transduced with rat RhebS16H [65] or empty plasmid and cultured in DMEM with 10% FBS and 1 μg/ml Puromycin for selection. Glucose-free DMEM was purchased from Gibco™ (Cat#11966025). 100 nM Bafilomycin A1 was used for 2 hr to inhibit autophagosome degradation.

CRISPR knockout of Atg7 and AMPKα1 in MEF cells

Two pairs of sgRNA targeting Atg7 (#1, 5’-TGGACACCAGGGAGAGCCGG-3’ and #2, 5’-GAACGAGTACCGCCTGGACG-3’) and two pairs of sgRNA targeting AMPKα1 (#1, 5’-TTATTGTCACAGGCATATGG-3’ and #2, 5’-GTGGGCAAGCACGAGTTGAC-3’) were subcloned into lentiCRISPR v2 (Addgene, #52961) according to the protocol in Dr. Feng Zhang’s lab. These two CRIPSR plasmids were packaged into lentiviruses with psPax2 and pMD2.G in HEK293 cells using the calcium phosphate method. MEF cells were infected with CRISPR lentiviruses and selected with Puromycin (2 – 4 μg/ml) for one week. Single clones were screened by limited dilution in 96-well plate. The selected clones were cultured in DMEM with 10% FBS.

Virus production and infection

Human scrambled shRNA, FIP200 shRNA, and Tsc1 shRNA encoded in pGIPZ lentiviral vector were purchased from Open Biosystems (Lafayette, CO). Mouse scrambled shRNA, LAL shRNA #1 and #2 were purchased from Sigma. Package vectors of pSPAX2 and pMD2.G were mixed with shRNA vectors and transfected in HK293 cells for virus production essentially as described before[37].

Neurosphere formation assay and in vitro differentiation

Neurospheres were cultured in neurobasal medium supplemented with B27 (Invitrogen, CA), 10 ng/ml basic fibroblast growth factor (bFGF) and 20 ng/ml epidermal growth factor (EGF) (Invitrogen, CA) in Ultra-Low Attachment dishes (Corning, MA), essentially as described in our previous reports [37, 38]. Neurospheres with diameter larger than 50 μm were counted 7–9 days after culturing. For their passage, primary neurospheres were collected by centrifugation, then incubated in 0.2% Trypsin at 37°C for 10 min with ~50 times pipetting. After addition of trypsin inhibitor supplemented with DNase I (Worthington, NJ) to stop digestion, dispersed cells were collected by centrifugation at 400 *g* for 10 minutes, counted, and cultured for secondary neurosphere formation and quantified as described before [37, 38]. In some experiments, the dispersed cells from neurospheres were cultured for differentiation in neurobasal medium supplemented with B27 (Invitrogen, CA), 10 ng/ml bFGF, and 5% (v/v) FBS in 48-well plates coated with 150 μg/ml poly-D-lysine (Biomedical Technologies, MA) and 20 μg/ml laminin (Invitrogen, CA) for another 7 or 14 days. Differentiated cells were fixed in 4% PFA for 30 min and then washed twice in cold PBS for 10 min. These cells were stained with β-III tubulin, NeuN, GFAP, MBP and DAPI for lineage analysis.

Antibodies and reagents

Mouse anti-Nestin (Cat: Rat-401, PMID: 23403289, DSHB, IA), IHC, 1:50; anti-GFAP (Cat# 3607, PMID: 28794441, Cell Signaling, MA), IHC, 1:100; anti-mTOR (Cat#: 14–2190-82, PMID: 18803507, ThermoFischer Scientific, CA), IF, 1:100; Alexa 647 conjugated anti-BrdU (Cat: B35133, PMID: 28754836, ThermoFischer Scientific, CA), IHC, 1:50; anti-beta-actin (Cat: A2228, PMID: 21498634, Sigma, MO), WB, 1:4,000; anti-GAPDH (Cat: G8795, PMID: 23222489, Sigma, MO), WB, 1:10,000; anti-vinculin (Cat:V9264, PMID: 23685627, Sigma, MO), WB, 1:5,000; anti-NeuN (Cat: MAB377, PMID: 26373451, Millipore, MA), IHC, 1:500. rabbit anti-Ki67 (Cat: M3060, PMID: 26402841, Spring Bioscience, CA), IHC, 1:200; anti-p62 (Cat: BML-PW9860, PMID: 22562096, Enzo, PA), WB, 1:1,000, IHC, 1:200; anti-GFAP (Cat: Z0334, PMID: 8229641, DAKO, CA), IHC, 1:200; anti-phosphorylated (Ser65) 4EBP1 (Cat: 9451, PMID: 28778941,Cell Signaling, MA), WB, 1:1,000; anti-phosphorylated (Thr37/46) 4EBP1 (Cat: 2855, PMID: 26913956,Cell Signaling, MA), IHC, 1:100, WB, 1:1,000; anti total 4EBP1 (Cat: 9644, PMID: 29720666, Cell Signaling, MA), WB, 1:1,000; anti-FIP200 (Cat: 12436, PMID: 27305347, Cell Signaling, MA), WB, 1:1,000; anti-beta-III tubulin (Cat: 5568, PMID: 25726526, Cell Signaling, MA), IF, 1:100; anti-NG2 (Cat: AB5320, PMID: 25902404, Millipore, MA), IHC, 1:100; anti-phosphorylated (Thr202/Tyr204) ERK1/2 (Cat: 4307, PMID: 22027685,Cell Signaling, MA), IHC, 1:100; anti-phosphorylated S6 kinase (Thr389) (Cat: 9234, PMID: 28928465, Cell Signaling, MA), WB, 1:1,000; anti total S6 kinase (Cat: 2708, PMID: 28835610, Cell Signaling, MA), WB, 1:1,000; anti-phosphorylated S6 ribosomal protein (Ser240/244) (Cat: 5364, PMID: 27026523, Cell Signaling, MA), IHC, 1:500, WB, 1:3,000; anti total S6 ribosomal protein (Cat: 2317, PMID: 29162813, Cell Signaling, MA), WB, 1:3,000; anti-LC3 (Cat: 2775, PMID: 28674081, Cell Signaling, MA), IF, 1:100, WB, 1:1,000; anti-phosphorylated (Ser473) pAKT (Cat:4060, PMID: 24670654, Cell Signaling, MA), IHC, 1:100; anti-phosphorylated-AMPK (Thr172)(Cat: 2535, PMID: 27409632, Cell Signaling, MA), IHC, 1:100, WB, 1:1,000; anti AMPK (Cat: 5831, PMID: 27172265, Cell Signaling, MA), WB, 1:1,000; anti-phosphorylated-Raptor (Ser792)(Cat: 2083, PMID: 23352126, Cell Signaling, MA), WB, 1:1,000; anti total Raptor (Cat: 2280, PMID: 28613987, Cell Signaling, MA), WB, 1:1,000; anti-phosphorylated-ACC (Ser79) (Cat: 3661, PMID: 28552492, Cell Signaling, MA), IHC, 1:100, WB, 1:1,000; anti total ACC (Cat: 3662, PMID: 28552492, Cell Signaling, MA), WB, 1:1,000; anti-pjosphorylated-Ulk1 (Ser757) (Cat: 6888, PMID: 30784596, Cell Signaling, MA), WB, 1:1,000; anti-pjosphorylated-Ulk1 (Ser555) (Cat: 5869, PMID: 30957628, Cell Signaling, MA), WB, 1:1,000; anti-Ulk1 (Cat: 8054, PMID: 30957628, Cell Signaling, MA), WB, 1:1,000; anti-SOX2 (Cat: AB5603, PMID: 25580734, Millipore, MA), IHC, 1:500; anti-LAL (Cat: ab154356, PMID: 26134519, Abcam, MA); WB, 1:2,000. Rat anti-Ki67 (Cat: 652402, PMID: 25675507, Biolegend, CA), IHC, 1:200; anti-MBP (Cat: MAB386, PMID: 25706475, Millipore, MA), IHC, 1:200; anti-LAMP2 (Cat: H4B4, PMID: 16874023, DSHB, IA), IF, 1:100. Guinee pig anti-DCX (Cat: Ab2253, PMID: 24880216, Millipore, MA), IHC, 1:500. Secondary antibodies: Anti-mouse IgG, HRP-linked Antibody (Cat: 7076, Cell Signaling MA); 1:10,000; Anti-rabbit IgG, HRP-linked Antibody (Cat: 7074, Cell Signaling MA); 1:10,000; AffiniPure Donkey Anti-Mouse IgG (H+L) (Jackson Immunology, PA); conjugated FITC Cat: 715–095-150; conjugated TRITC, Cat: 715–025-150; IF and IHC, 1:200; AffiniPure Donkey Anti-Rabbit IgG (H+L) (Jackson Immunology, PA); conjugated FITC Cat: 711–095-152; conjugated TRITC, Cat:711–025-152; IF and IHC, 1:200; AffiniPure Donkey Anti-Rat IgG (H+L) (Jackson Immunology, PA); conjugated FITC Cat: 712–095-153; conjugated TRITC, Cat: 712–025-153; IF and IHC, 1:200; AffiniPure Goat Anti-Guinea Pig IgG (H+L) (Jackson Immunology, PA); conjugated TRITC, Cat: 106–025-033; IHC, 1:200.

BODIPY 493/503 was purchased from Invitrogen (Invitrogen, CA). DAPI was purchased from Millipore (Millipore, CA). DMEM, glucose-free DMEM and HBSS were from Thermo Fischer Scientific. ATP, BSA, palmitate, octanoate, glucose, glutamine, sodium pyruvate, Bafilomycin A1, chloroquine and Spautin1 were purchased from Sigma (St Louis, MO).2DG, Orlistat, Atglistat, JZL, etomoxir, ranolazine, and trimetazidine were purchased from Cayman (Ann Arbor, MI); rapamycin was from LC laboratory.

Histology, immunofluorescence (IF) and BODIPY (493/503) staining

Mice were euthanized using CO_2, and a complete tissue set was harvested during necropsy. The weight of brains was measured before fixation. Fixation was carried out for 16 hr at 4°C using 4% (w/v) freshly made, pre-chilled PBS-buffered paraformaldehyde (PFA). The brain tissues were all and embedded in paraffin and sagittal sectioned at 5 μm sections. Slides from histologically comparable positions (triangular lateral ventricle with intact RMS) were stained with hematoxylin and eosin (H&E) for routine histological examination or left unstained for immunofluorescence (IF). H&E stained sections were examined under a BX41 light microscope (Olympus America, Inc., Center Valley, PA), and images were captured with an Olympus digital camera (model DP70) using DP Controller software (Version 1.2.1.10 8). For immunofluorescence, unstained tissues were first deparaffinized in 3 washes of xylene (3 min each) and then rehydrated in graded ethanol solutions (100, 95, 70, 50, and 30%). After heat-activated antigen retrieval (Retriever 2000, PickCell Laboratories B.V., Amsterdam, Holland) according to the manufacturer’s specifications, sections were treated with Protein Block Serum Free (Dako Corp, CA) at room temperature for 10 min. Slices were then incubated with primary antibodies at 4°C for 16 hr in a humidified chamber, washed in PBS 3 times (5 min each) and incubated with the 1:200 secondary antibodies for 1 hr at room temperature. After secondary antibody incubation, slides are washed in PBS 3 times (5 min each). Nuclei were stained with DAPI and mounted with Vectashield mounting medium (Vector Laboratories, CA). Digital photography was carried out as described previously[62].

For BODIPY staining, a fresh solution of BODIPY was diluted in PBS at a concentration of 1μg/mL and applied to 4% PFA fixed samples. After PFA was removed by three washes with PBS, samples were incubated in 1 μg/ml BODIPY 493/503 for 20 min at room temperature. Some samples were also labeled with antibodies (LAMP2 and LC3) to identify lysosome and autophagosomes in cells. The samples were observed using a Zeiss LSM 700 confocal microscope (Carl Zeiss).

Colocalization of mTOR with lysosomal marker LAMP2 was quantitated using Pearson's correlation coefficient (PCC). Confocal acquired imaging data were analyzed using the Coloc 2 plugin of the Fiji distribution of ImageJ software (http://imagej.net/Coloc_2). Cells were selected as regions of interest (ROIs) using the freehand selection tool. Pearson's R value (no threshold) reported in the ImageJ Log window was recorded. Values shown represent mean ± SE (5 independent experiments from at least 30 cells).

Oil Red O staining

25 μm frozen brain sections were washed with 60% 2-propanol (Fisher), incubated in filtered 0.3% Oil Red O (Allied Chemical) for 10 min, then rinsed in 60% 2-propanol followed by one rinse with distilled H_2O. All samples were mounted in Vectashield, covered with glass cover slips (No. 1, VWR), and mounted with Permount (Biomeda, CA).

BrdU incorporation assay and TUNEL assay

For in vivo studies, BrdU was administrated intra-peritoneally (I.P.) at 100 μg/gram for 3 times at 2 hr intervals. Mice were either euthanized 2 hr after the last injection (short term incorporation) or 2 weeks later (long term retention), and tissues were processed as described above. For BrdU detection, the samples were treated with 2 M HCL at room temperature for 20 min to denature nucleotides, then neutralized with 0.1 M sodium borate at room temperature for another 20 min. After 3 washes in PBS (5 min each), slides were incubated with mouse anti-BrdU antibody and secondary antibodies as described in immunofluorescent staining. Nuclei were stained with DAPI and mounted with Vectashield mounting medium (Vector Laboratories, CA). For IF and detection of BrdU in the same tissue, IF was carried out first and samples were post-fixed with 4% PFA at room temperature for 20 min before nucleotide denaturing with HCL. Histological examination and digital photography were carried out as described above.

Apoptotic cells were detected by TUNEL according to the protocol provided by the manufacture in the In Situ Cell Death Detection Kit-TMR Red (Roche, Germany).

Cellular ATP content measurement

Intracellular ATP level was measured by using CellTiter-Glo® Luminescent Cell Viability Assay Kit (Promega, WI). ATP dissolved in DMEM was used as standards of 5 μM, 500 nM, 50 nM, and 5 nM. The experimental procedure was provided by the manufacture in the kit. 10,000 cells were used for each well and 3 wells were used for each sample. The measurement was carried out on a Synergy™ 2 Multi-Mode Microplate Reader (BioTEK, VT).

Measurement of β-oxidation

β-oxidation was measured using a ^{3}H-palmitate adapted from a previous publication (Djouadiet al., 2003 Mol Genet Metab). Briefly, 5×10^5 MEF were washed with glucose-free DMEM, then cultured with 400 μl of (9,10-^{3}H) Palmitate:albumin for 2 hrs under glucose-free conditions at 37°C. After incubation, 10% TCA was added to each tube and centrifuged at 3300 rpm for 10 min at 4°C, then mixed with 6N NaOH and applied to ion-exchange columns. The column was washed with 1 mL of water and the eluates were counted using a scintillation counter.

Measurement of triglyceride, FFA and glycerol release

MEFs (4×10^6) were lysed in 0.2 ml lysis buffer (5% NP40 in H_2O) and assayed for triglyceride using a Triglyceride Quantification Colorimetric Kit (Biovision Inc, CA) according to the manufacturer’s instructions. Samples were twice heated to 90°C for 2 min and cooled to room temperature, then centrifuged to remove any insoluble material, and diluted twofold in Triglyceride Assay Buffer. Samples were then incubated with lipase for 20 min, followed by a 30-min incubation with Triglyceride Reaction Mix. The OD at 570 nm was measured and triglyceride amount was calculated using a standard curve.

MEF (2×10^6) cells were extracted by homogenization with 200 μl of chloroform-Triton X-100 (1% Triton X-100 in pure chloroform) in a microhomogenizer and assayed for FFA using a Free Fatty Acid Quantification Colorimetric/Fluorometric Kit (Biovision Inc. CA). Extracts were spun for 5–10 minutes at top speed in a microcentrifuge. The organic phase (lower phase), was collected, air dried at 50°C to remove chloroform, and vacuum dried 30 min to remove trace chloroform. The dried lipids (in Triton X-100) are dissolved in 200 μl of Fatty Acid Assay Buffer by vortexing extensively for 5 min. The extraction procedure can be proportionally scaled up if a larger amount of sample is desired. 1– 50 μl of the extracted sample is used per assay.

Glycerol in MEF supernatants was measured using absorbance at 570 nm with a Free Glycerol Colorimetric/Fluorometric Assay Kit (Biovision Inc. CA) by comparison to a glycerol standard in according to the protocol provided by the manufacture.

2DG, CQ, ETO, Rano, TMZ and rapamycin administration

PBS, 2DG (500 mg/kg in PBS), CQ (50 mg/kg in PBS), 2DG+CQ, ETO (50 mg/kg in PBS), Rano (25 mg/kg in PBS), TMZ (5 mg/kg in PBS), 2DG+ETO, 2DG+Rano, 2DG+TMZ were administrated intra-peritoneal (IP) into *Tsc1*^{GFAP} cKO mice every other day from P7 for 14 days. Ctrl mice were injected with 2DG+CQ, 2DG+ETO, 2DG+Rano, 2DG+TMZ at same frequency from P7 to P21. For administration of rapamycin (LC lab), freshly prepared rapamycin (Sun et al., 2015) was IP injected into Ctrl and *FIP200*^{hGFAP} cKO mice at a dose of 2.5 mg/kg once a day from P5 to P21. After treatment, mice were euthanized as described previously and analyzed for histological changes.

Analysis of murine subependymal nodules (SEN)-like structure

We analyzed the SEN-like structures by H&E staining of brain samples from P7, P14, P21, and P28 mice. The slides from the start point to the end point of lateral ventricle were examined at an interval of 30–40 μm under both high and low magnifications. Each slide containing 3–4 slices of brain sections. The lateral ventricle and surrounding striatum, CC, hippocampus, and cortex from Ctrl, FIP200 cKO, Tsc1 cKO, and FIP200/Tsc1 2cKO mice at P21 were examined. Brain slides from P21 Tsc1 cKO mice receiving vehicles, 2DG, CQ, 2DG + CQ, beta-oxidation inhibitors, 2DG + beta-oxidation inhibitors and P21 Ctrl mice receiving 2DG + CQ, as well as 2DG + beta-oxidation inhibitors were examined.

Protein extraction, SDS-PAGE and immunoblotting

Cells were used for protein extraction by homogenization in modified radioimmune precipitation assay buffer (50 mm Tris-HCl, pH 7.4, 1% Triton X-100, 0.2% sodium deoxycholate, 0.2% SDS, 1 mm sodium EDTA) supplemented with protease inhibitors (5 μg/ml leupeptin, 5 μg/ml aprotinin, and 1 mm phenylmethylsulfonyl fluoride). After removing cell debris by centrifugation at 13,000 rpm for 10 min at 4°C, protein concentration was determined using Bio-Rad protein assay reagent. The lysates were boiled for 5 min in 1×SDS sample buffer (50 mm Tris-HCl, pH 6.8, 12.5% glycerol, 1% SDS, 0.01% bromphenol blue) containing 5% β-mercaptoethanol. They were then analyzed by SDS-PAGE followed by immunoblotting using various antibodies, as described previously (Wang et al., 2013, 2016).

Seahorse extracellular assay for oxygen consumption rate (OCR)

Measurement of OCR by XF24 microplate-based respirometry from intact cells was made using an XF24 Extracellular Flux Analyzer (Seahorse Bioscience, MA). 20,000 cells per well were seeded in Seahorse 24-well XF Cell Culture Microplates and incubated overnight at 37°C with 5% CO_2. Mitochondria stress tests were initiated according to the manufacturer's instructions by replacing the growth medium in each well with 500 μl of Seahorse XF Base Medium (supplemented with 10 mM glucose, 2 mM L-glutamine, and 1 mM sodium pyruvate for normal conditions, or without glucose only for glucose deprivation conditions) pre-warmed at 37°C. Glycolysis inhibitor 2DG (10 mM) was included in Seahorse XF Base media for some experiments. Cells were then incubated at 37 °C in a non-CO2 incubator for 60 min to allow temperature and pH equilibration. Following the equilibration period, cells were loaded into the XF24 extracellular flux analyzer and further equilibrated for 20 min prior to the first measurement. After an OCR baseline measurement, the minimum oxygen consumption was determined by injection of 4 μM oligomycin (Olig) and sequentially the maximal respiration rate was assessed upon injection of 0.5 μM FCCP (Trifluoromethoxy carbonylcyanide phenylhydrazone). Finally, the non-mitochondrial oxygen consumption was evaluated after injection of both 0.5 μM rotenone and antimycin (R/A). The measurements were normalized to cell number, which were quantified using CyQuant DNA dye (Invitrogen). Analysis of data was carried out using Wave software and the XF Mito/Glycolysis stress test report generator (Seahorse Bioscience).

Spautin1 (10 μM) and chloroquine (20 μM) were incubated with cells overnight before experiments. ETO, Rano or TMZ prepared in assay medium (75 μl) were preloaded into reagent delivery chambers. The assay medium final working concentration (200 μM ETO, 400 μM Rano, or 1 mM TMZ) was injected after FCCP and OCR was measured 3 times before injection of rotenone and antimycin.

Statistical analysis

Lengths, areas, and the number of cells from comparable sections were quantified using the ImageJ software package. Statistical significance was evaluated by Student's t-test, one way ANOVA, two way ANOVA, and Pearson correlation coefficient, and differences between groups for frequency of SEN-like structures were performed using ELDA, as described previously[66], with $p<0.05$ as indicative of statistical significance using Graph Pad Prism (Version 5.0). The number of animals used for quantification was indicated in the figure legends.

Extended Data

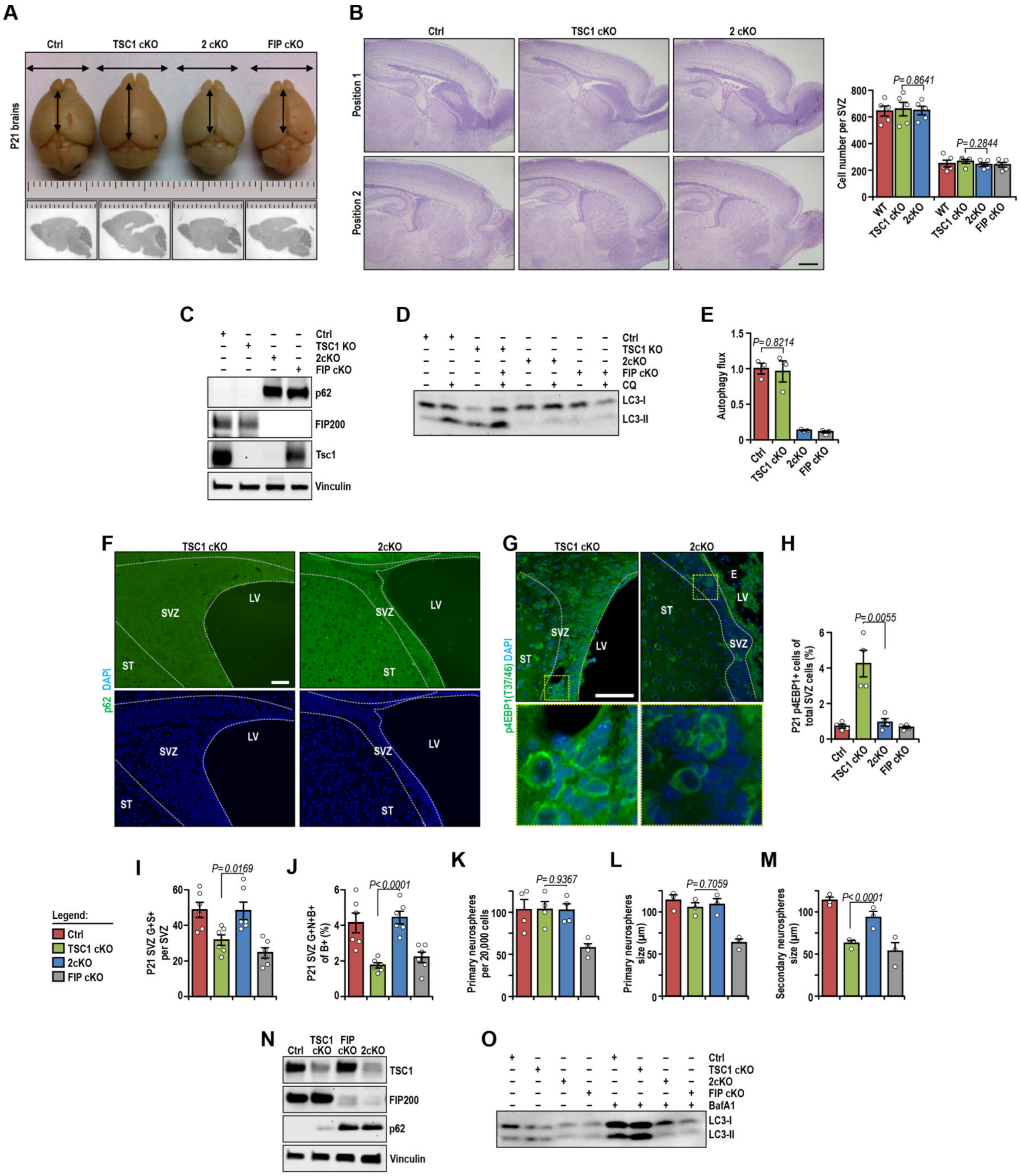

Extended Data Fig. 1. Analyses of autophagy, mTORC1 signaling and NSCs from SVZ tissues and neurospheres.

(A) Brain size (upper panel) and H&E staining of sagittal sectioned brain (lower panel) of Ctrl, *Tsc1*^{GFAP} cKO, 2cKO, and *FIP200*^{GFAP} cKO mice at P21. Five independent experiments gave similar results.

(B) H&E staining of sagittal sectioned brain at two positions of Ctrl, *Tsc1*^{GFAP} cKO, 2cKO, and *FIP200*^{GFAP} cKO mice at P0. Mean ± SE of the number of SVZ cells in Ctrl, *Tsc1*^{GFAP} cKO, 2cKO, and *FIP200*^{GFAP} cKO mice at P0 shown on the right. n = 5 independent experiments.

(C and D) The levels of p62, FIP200 and Tsc1 (C) and LC3 (D) in isolated SVZ tissue of Ctrl, *Tsc1*^{GFAP}cKO, 2cKO, and *FIP200*^{GFAP}cKO mice treated with or without CQ for 14 days. Three independent experiments gave similar results.

(E) Means ± S.E. of the autophagy flux (calculated as LC3-II with CQ divided by LC3-II without CQ as shown in B). n = 3 independent experiments.

(F, G) Immunofluorescence of p62 (F), p4EBP1 (phosphorylated at T37/46) (G), and DAPI in SVZ of *Tsc1*^{GFAP} cKO and 2cKO mice at P21. Bottom panels in G show details of p4EBP1$^+$ cells in boxed area.

(H) Mean ± SE of the percentage of p4EBP1$^+$cells in SVZ of Ctrl, *Tsc1*^{GFAP} cKO, 2cKO, and *FIP200*^{GFAP} cKO mice at P21. n = 4 independent experiments.

(I-J) Mean ± SE of the number of GFAP$^+$Sox2$^+$NSC (I) and the number of GFAP$^+$Nestin$^+$BrdU$^+$ cells of total BrdU$^+$ cells (J) in SVZ of Ctrl, *Tsc1*^{GFAP} cKO, 2cKO, and *FIP200*^{GFAP} cKO mice at P21. n = 6 independent experiments.

(K-M) Mean ± SE of the number (K) and size (L and M) of primary (K and L) and secondary (M) neurospheres from SVZ cells of Ctrl, *Tsc1*^{GFAP} cKO, 2cKO, and *FIP200*^{GFAP} cKO mice at P21. n = 4 (K), 3 (L, M) independent experiments.

(N) Lysates from primary neurospheres of Ctrl, *Tsc1*^{GFAP}cKO, 2cKO, and *FIP200*^{GFAP}cKO mice examined by immunoblotting with indicated antibodies. Three independent experiments gave similar results.

(O) The level of LC3 in neurospheres of Ctrl, *Tsc1*^{GFAP}cKO, 2cKO, and *FIP200*^{GFAP}cKO mice treated with or without BafA1. Three independent experiments gave similar results.

The dotted lines indicated the boundaries of SVZ with LV (F and G). E: ependymal layer; LV: lateral ventricle; ST: striatum; SVZ: subventricular zone.

Bar = 100 μm. Data were analyzed by one-way ANOVA with Tukey's post-hoc test (B, E, H-M).

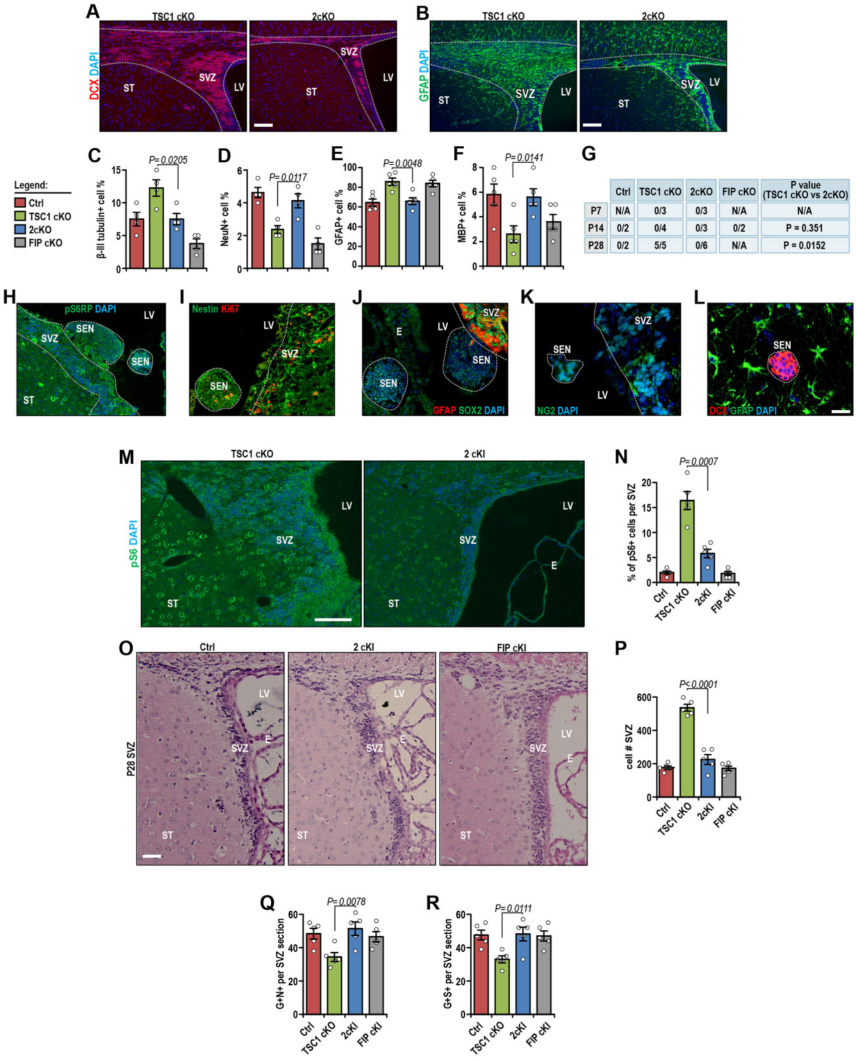

	Ctrl	TSC1 cKO	2cKO	FIP cKO	P value (TSC1 cKO vs 2cKO)
P7	N/A	0/3	0/3	N/A	N/A
P14	0/2	0/4	0/3	0/2	P = 0.351
P28	0/2	5/5	0/6	N/A	P = 0.0152

Extended Data Fig. 2. FIP200 Knockout and FIP200-4A Knockin mutant rescued defective phenotypes in *Tsc1*^{GFAP} cKO SVZ.

(A, B) Immunofluorescence of DCX (A), GFAP (B), and DAPI in SVZ of *Tsc1*^{GFAP} cKO and 2cKO mice at P21. Four independent experiments gave similar results.

(C-F) Mean ± SE of the percentage of β-III tubulin^{+} cells (C), NeuN^{+} cells (D), GFAP^{+} cells (E) and MBP^{+} cells (F) from differentiated neurospheres of Ctrl, *Tsc1*^{GFAP}cKO, 2cKO, and *FIP200*^{GFAP}cKO mice. n = 4 (C, D), 5 (E, F) independent experiments.

(G) Frequency of SEN-like structure in Ctrl, *Tsc1*^{GFAP} cKO, 2cKO, 2cKI, and*FIP200*^{GFAP}cKO mice at P7, P14, and P28. Animal number is indicated in the figure.

(H-L) Immunofluorescence of pS6RP (H), nestin and Ki67 (I), GFAP and Sox2 (J), NG2 (K), DCX and GFAP (L) in SEN-like lesion in *Tsc1*^{GFAP} cKO brain at P21. Three independent experiments gave similar results.

(M) Immunofluorescence of pS6RP and DAPI in SVZ of *Tsc1*^{GFAP} cKO and 2cKI mice at P21. Five independent experiments gave similar results.

(N) Mean ± SE of the number of pS6RP^{+}cells in SVZ of Ctrl, *Tsc1*^{GFAP} cKO, 2cKI, and *FIP200*^{GFAP} cKI mice at P21. n = 5 independent experiments.

(O) H&E staining of SVZ from Ctrl, 2cKI, and *FIP200*^{GFAP} cKI mice at P28. Five independent experiments gave similar results.

(P) Mean ± SE of SVZ cell number of Ctrl, *Tsc1*^{GFAP} cKO, 2cKI, and *FIP200*^{GFAP} cKI mice at P21. n = 5 independent experiments.

(Q, R) Mean ± SE of the number of GFAP$^+$Nestin$^+$ NSC (Q) and GFAP$^+$Sox2$^+$ NSC (R) in SVZ of Ctrl, *Tsc1*^{GFAP} cKO, 2cKI, and *FIP200*^{GFAP} cKI mice at P21. n = 5 independent experiments.

The dotted lines indicated the boundaries of SVZ or SEN-like lesion with LV. E: ependymal layer; LV: lateral ventricle; SEN: subependymal nodule-like lesion; ST: striatum; SVZ: subventricular zone. Bar = 100 μm (A, B, M, O), 40 μm (H-L). Data were analyzed by one-way ANOVA with Tukey's post-hoc test (C-F, N, P-R), Chi-Square test (G).

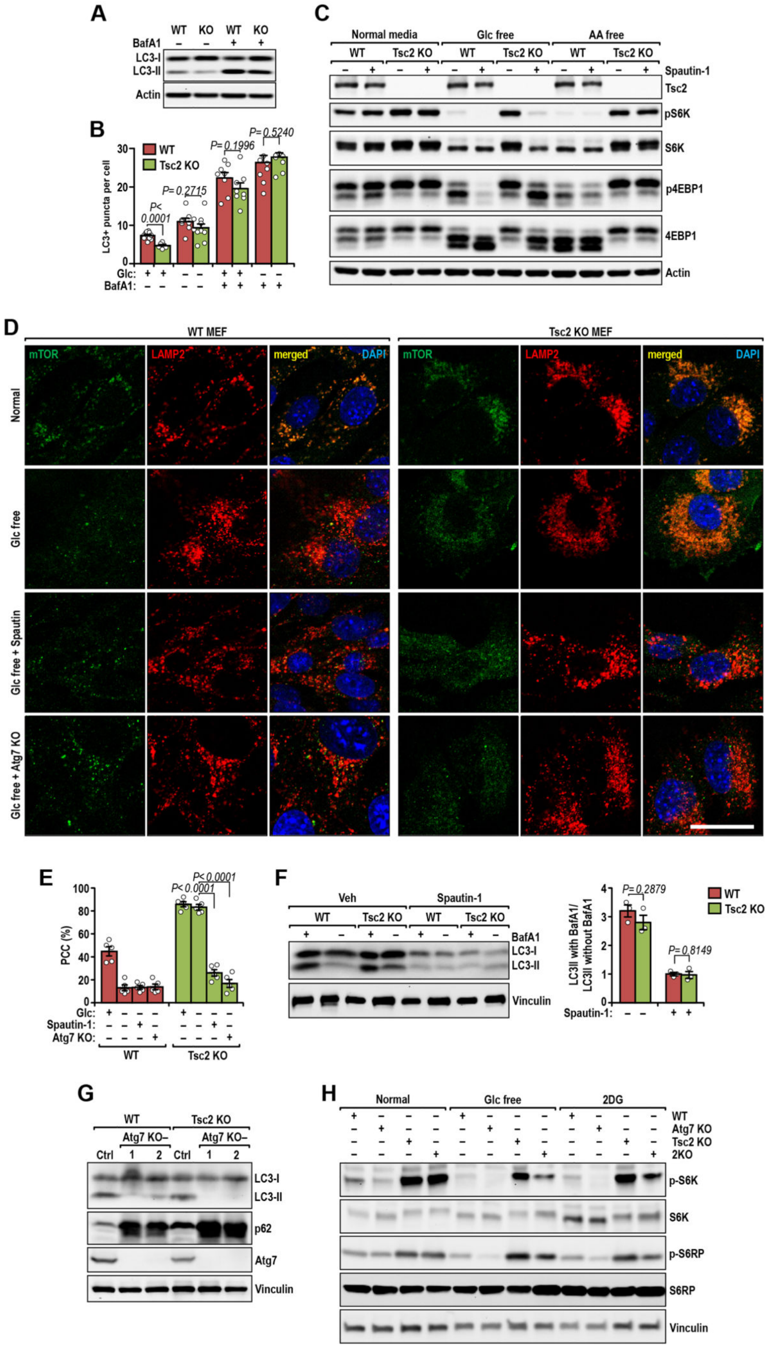

Extended Data Fig. 3. Autophagy sustained mTORC1 hyper-activation in Tsc-deficient MEF under energy stresses.

(A) Lysates from WT and Tsc2 KO MEF treated with DMSO or BafA1 examined by immunoblots with antibodies for LC3 and actin. Three independent experiments gave similar results.

(B) Mean ± SE of the number of LC3 puncta of DMSO or Spautin1 treated WT and Tsc2 KO MEF in normal media and glucose-free media (without FBS) with or without BafA1 for 2 hours. Spautin1 was pre-incubated for 12 hours. n = 6 – 12 independent experiments for at least 200 cells.

(C) Lysates from DMSO or Spautin1 treated WT MEF and Tsc2 KO MEF under normal, glucose-free, and amino acid-free conditions (without FBS) for 2 hours were examined with indicated antibodies. Spautin1 was pre-incubated for 12 hr. Three independent experiments gave similar results.

(D) Immunofluorescence of mTOR, LAMP2 and DAPI in WT MEF, Tsc2 KO MEF, and Tsc2/Atg7 2KO MEF under normal media (without FBS), glucose-free media (without FBS, or glucose-free media with 10 μM Spautin1 (without FBS) for 2 hours. Spautin1 was pre-incubated for 12 hr. Four independent experiments gave similar results.

(E) Mean ± SE of the Pearson correlation coefficient (PCC) of mTOR co-localization on $LAMP2^+$ structure in WT MEF, Atg7 KO MEF, Tsc2 KO MEF, and 2KO MEF under normal media, glucose-free media, and glucose-free media (without FBS) with Spautin1 for 2 hours. n = 5 independent experiments for at least 200 cells.

(F) Lysates from WT MEF and Tsc2 KO MEF treated with DMSO or Spautin1 were examined by immunoblots with antibody for LC3 and Vinculin. BafA1 was used to block autophagosome degradation and Spautin1 was pre-incubated for 12 hours before experiments. Three independent experiments gave similar results. Mean ± SE of the relative level of LC3II of DMSO or Spautin1 treated WT MEF and Tsc2 KO MEF with or without BafA1 for 2 hours on the right. n = 3 independent experiments.

(G) Lysates from WT MEF, Atg7 KO MEF (2 independent clones), Tsc2 KO MEF, and 2KO MEF (2 independent clones) were examined by immunoblots with antibodies as indicated. Three independent experiments gave similar results.

(H) Lysates were extracted from WT MEF, Atg7 KO MEF (clone 1), Tsc2 KO MEF, and 2KO MEF (clone 1) in normal media, glucose-free media and 2DG supplemented media (without FBS) for 2 hours. The levels of phosphorylated S6K, total S6K, phosphorylated S6RP, total S6RP, and vinculin were examined. Three independent experiments gave similar results.

Bar = 10 μm. Data were analyzed by two-tailed Student's t test (B, F), Pearson correlation coefficient (E).

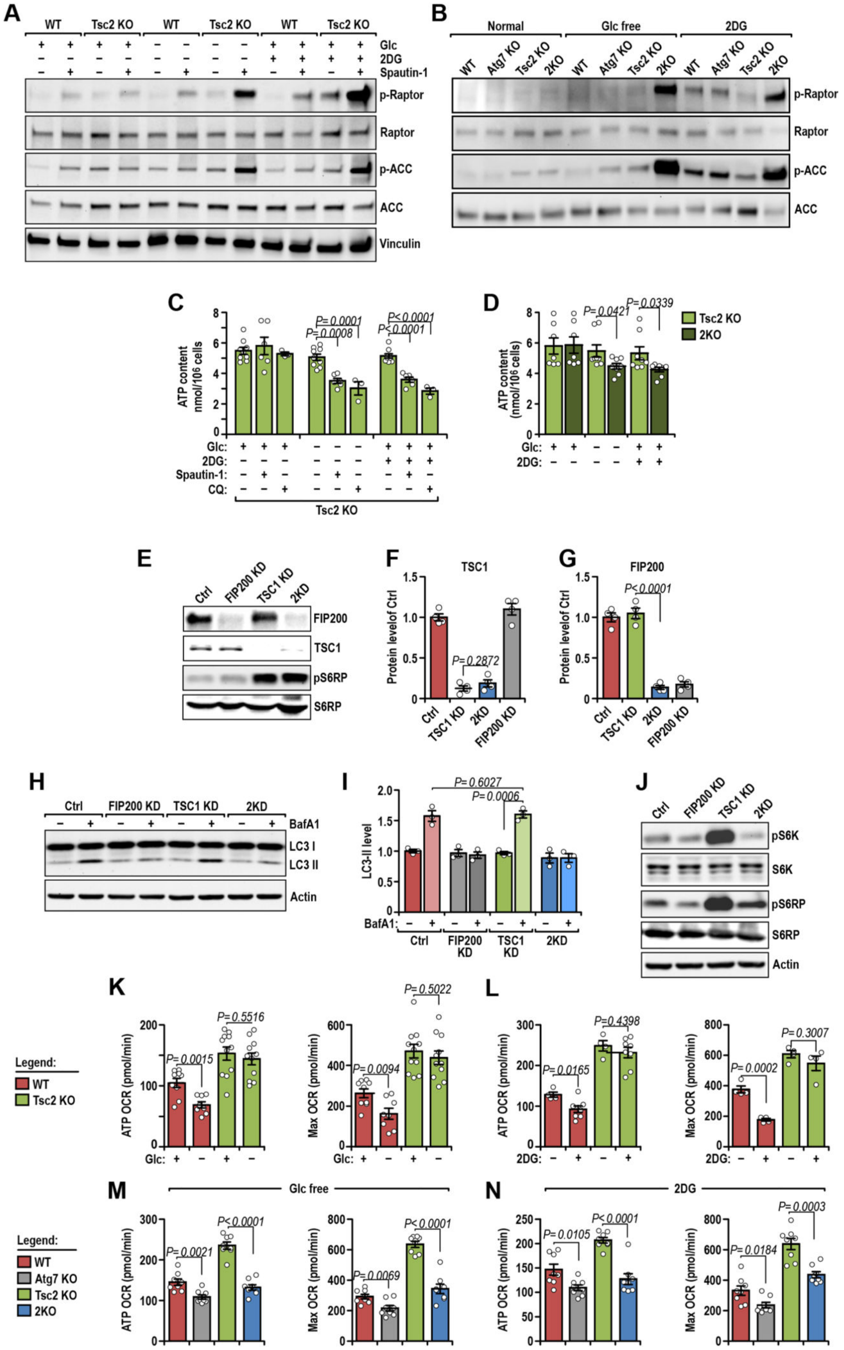

Extended Data Fig. 4. Analysis of the role of autophagy, TORC1 hyper-activation, ATP content and AMPK targeting phosphorylation in Tsc-deficient neurospheres, MEF, 293 cells, and SVZ

(A) Lysates extracted from WT and Tsc2 KO MEF in normal, glucose-free, and 2DG supplemented media (without FBS) for 2 hours were examined by immunoblot as indicated. Cells were pre-incubated with DMSO or 10 μM Spautin1 for 12 hours. Three independent experiments gave similar results.

(B) Lysates were extracted from WT, Atg7 KO, Tsc2 KO, and 2KO MEF in normal, glucose-free, and 2DG supplemented media (without FBS) for 2 hours. The levels of phosphorylated Raptor, total Raptor, phosphorylated ACC, and total ACC were examined. Three independent experiments gave similar results.

(C) Mean ± SE of the ATP content of Tsc2 KO MEF in normal, glucose-free, and 2DG supplemented media (without FBS) supplemented with 10 μM Spautin1 or 20 μM CQ for 2 hours was shown. The autophagy inhibitors were pre-incubated for 12 hr. n = 3 – 9 independent experiments.

(D) Mean ± SE of the ATP content of Tsc2 KO MEF and 2KO MEF in normal, glucose-free, and 2DG supplemented media (without FBS) for 2 hours. n = 7 – 8 independent experiments.

(E) Lysates from Ctrl, FIP200 KD, TSC1 KD, and 2KD 293 cells were examined by immunoblots with indicated antibodies. Four independent experiments gave similar results.

(F, G) Means ± S.E. of the protein levels of TSC1 (F) and FIP200 (G) in Ctrl, FIP200 KD, TSC1 KD, and 2KD 293 cells were shown. n = 4 independent experiments.

(H) The level of LC3-II was examined in Ctrl, FIP200 KD, TSC1 KD, and 2KD 293 cells treated with or without BafA1. Three independent experiments gave similar results.

(I) Mean ± S.E. of the level of LC3-II in Ctrl, FIP200 KD, TSC1 KD, and 2KD 293 cells treated with or without BafA1was shown. n = 3 independent experiments.

(J) Lysates prepared from Ctrl, FIP200 KD, TSC1 KD, and 2KD 293 cells treated with 25 mM 2DG (without FBS) for 2 hours and analyzed by immunoblot with antibodies as indicated. Three independent experiments gave similar results.

(K, L) Mean± SE of ATP related and maximum OCR in WT and Tsc2 KO MEF under normal or glucose-free conditions (K) and normal or 2DG treatment conditions (L). n = 9 – 11 (K) and 4 (L) independent experiments.

(M, N) Mean± SE of ATP related and maximum OCR in WT MEF, Atg7 KO MEF, Tsc2 KO MEF, and 2KO MEF under glucose-free conditions (M) and 2DG treatment conditions (N). n = 8 independent experiments.

Data were analyzed by two-tailed Student's t test (C, D, I, K-N), one-way ANOVA with Tukey's post-hoc test (F, G).

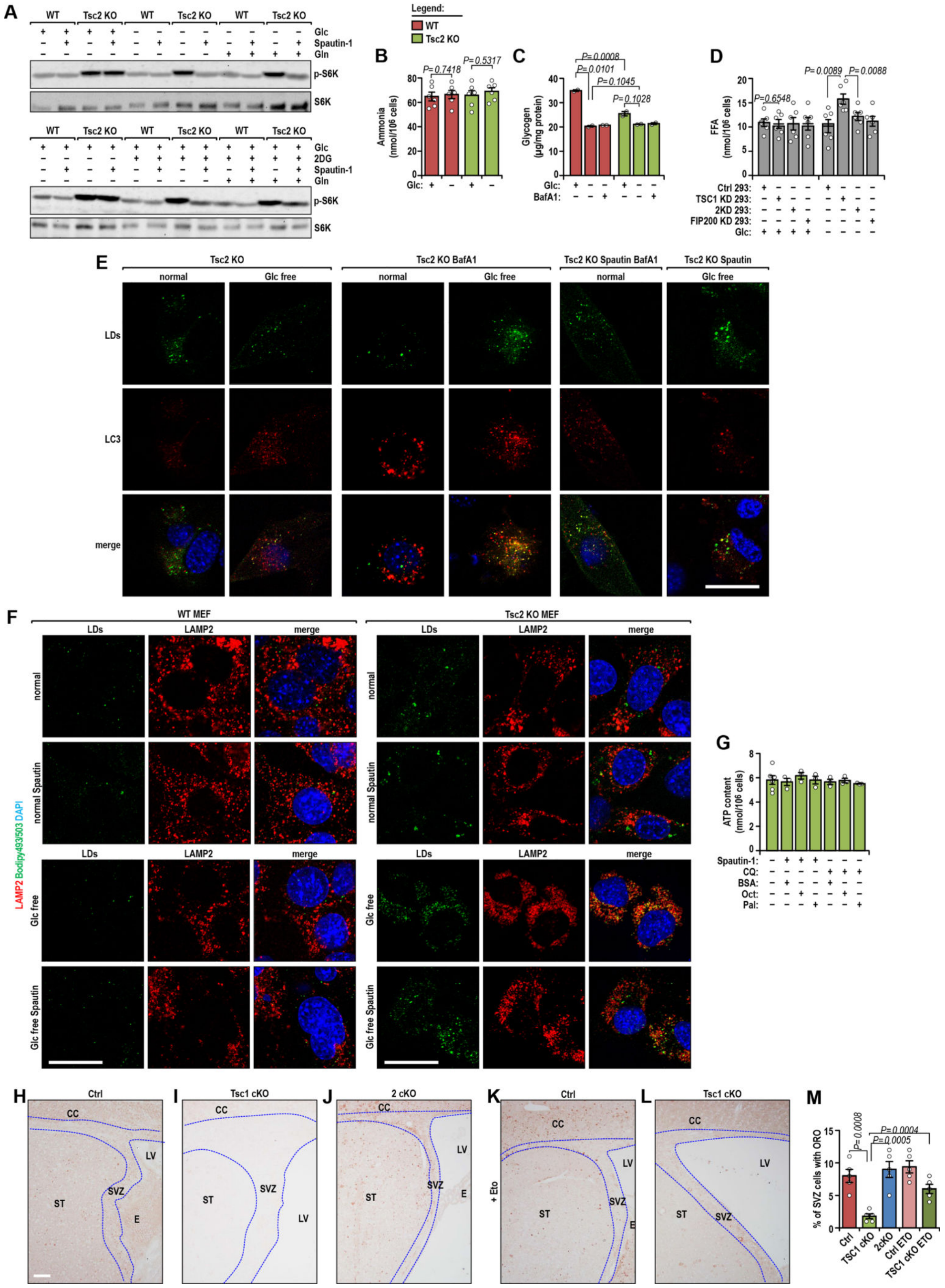

Extended Data Fig. 5. Energy stressed Tsc-deficient cells activated lipolysis through autophagy.

(A) Lysates were extracted from DMSO or Spautin1 treated WT and Tsc2 KO MEF supplemented with 20 mM glutamine under normal, glucose-free (upper panels), or 2DG treatment conditions (lower panels) for 2 hours. The levels of phosphorylated S6K and total S6K were examined by immunoblot with antibodies as indicated. Three independent experiments gave similar results.

(B, C) Mean ± SE of the ammonia content (B) and the glycogen content (C) in WT and Tsc2 KO MEF under normal and glucose-free media (for C, with or without BafA1 treatment) for 2 hours. n = 6 (B) and 2 (C) independent experiments.

(D) Mean ± SE of the content of FFAs in Ctrl, Tsc1 KD, 2KD, and FIP200 KD 293 cells under normal and glucose-free media. n = 6 independent experiments.

(E) Immunofluorescence for lipid droplets, LC3 and DAPI in DMSO, BafA1, and Spautin1 treated Tsc2 KO MEF under normal or glucose-free conditions (without FBS) for 2 hours. Four to nine independent experiments for at least 200 cells gave similar results.

(F) Immunofluorescence for LDs, LAMP2 and DAPI in DMSO or Spautin1 treated WT and Tsc2 KO MEF under normal or glucose-free conditions (without FBS) for 2 hours. Six to ten independent experiments for at least 200 cells gave similar results.

(G) Mean ± SE of ATP content in CQ or Spautin-1 treated Tsc2 KO MEF under normal conditions and supplemented with BSA or BSA-Palmitate for 2 hours. n = 3 – 6 independent experiments.

(H-L) Representative images of lipid droplets (indicated by Oil Red O staining) in SVZ of Ctrl (H and K), $Tsc1^{GFAP}$ cKO (I and L), and 2cKO (J) mice treated with (K and L) or without (H-J) ETO at P21. Five independent experiments gave similar results.

(M) Mean ± SE of the percentage of cells with lipid droplets in SVZ of Ctrl, $Tsc1^{GFAP}$ cKO, and 2cKO mice treated with or without ETO at P21. n = 5 independent experiments.

Bar = 10μm.Data were analyzed by two-tailed Student’s t test (B, D, G), one-way ANOVA with Tukey’s post-hoc test (C, M).

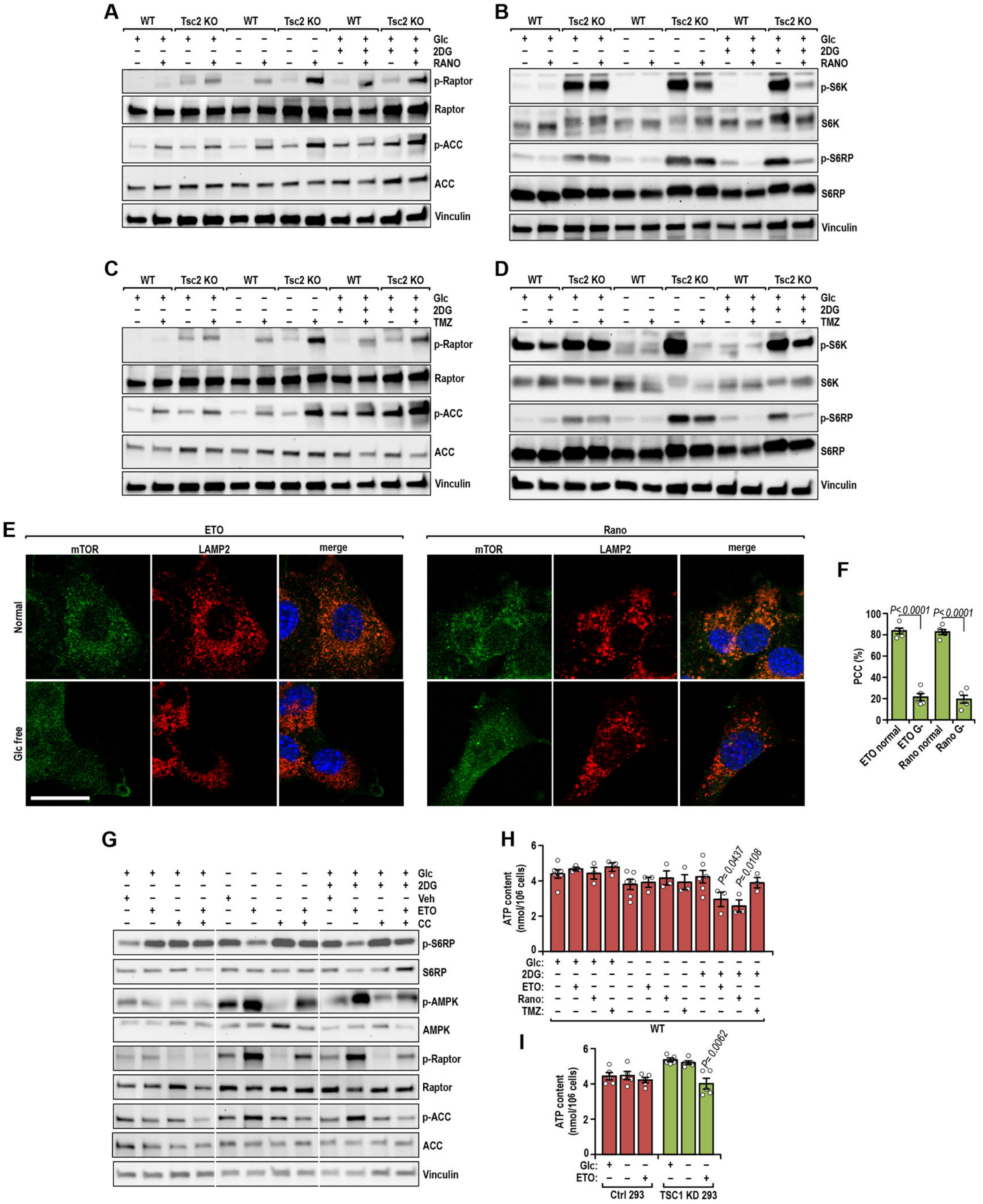

Extended Data Fig. 6. Regulation of activation of mTORC1, AMPK, and ATP content by inhibitors for β-oxidation and AMPK in energy-stressed Tsc-deficient cells.

(A-D) Lysates were extracted from WT MEF and Tsc2 KO MEF in normal media, glucose-free media and 2DG supplemented media (without FBS) for 2 hours. Cells were pre-incubated with β-oxidation inhibitors of Rano (A and B) and TMZ (C and D) for 12 hours and followed by 2 hours treatment. In (A and C), the levels of phosphorylated Raptor, total Raptor, phosphorylated ACC, total ACC, and vinculin were examined. In (B and D), the levels of phosphorylated S6K, total S6K, phosphorylated S6RP, total S6RP, and vinculin were examined. Three independent experiments gave similar results.

(E) Immunofluorescence of mTOR, LAMP2, and DAPI in ETO and Rano treated Tsc2 KO MEF under normal and glucose-free media for 2 hours. Five independent experiments for at least 200 cells gave similar results.

(F) Mean ± SE of the Pearson correlation coefficient of mTOR localization on LAMP2$^+$ structure in Tsc2 KO MEF treated with ETO or Rano under glucose-free conditions. n = 5 independent experiments.

(G) Lysates from vehicle, ETO, or Compound C (CC) treated Tsc2 KO MEF in normal media, glucose-free media, and 2DG supplemented media (without FBS) for 2 hours were examined by immunoblot using antibodies as indicated. Cells were pre-incubated with ETO with or without CC for 24 hours. Three independent experiments gave similar results.

(H) Mean ± SE of the ATP content of β-oxidation inhibitors of ETO, TMZ, and Rano treated WT MEF in normal media, glucose-free media, and 2DG media (without FBS) for 2 hours. The β-oxidation inhibitors were pre-incubated for 12 hours. n = 3 – 6 independent experiments.

(I) Mean ± SE of ATP content in ETO treated Ctrl and Tsc1 KD 293 cells under glucose deprivation conditions for 2 hours. n = 5 independent experiments.

Bar = 10 μm. Data were analyzed two-tailed Student’s t test (H, I), Pearson correlation coefficient (F).

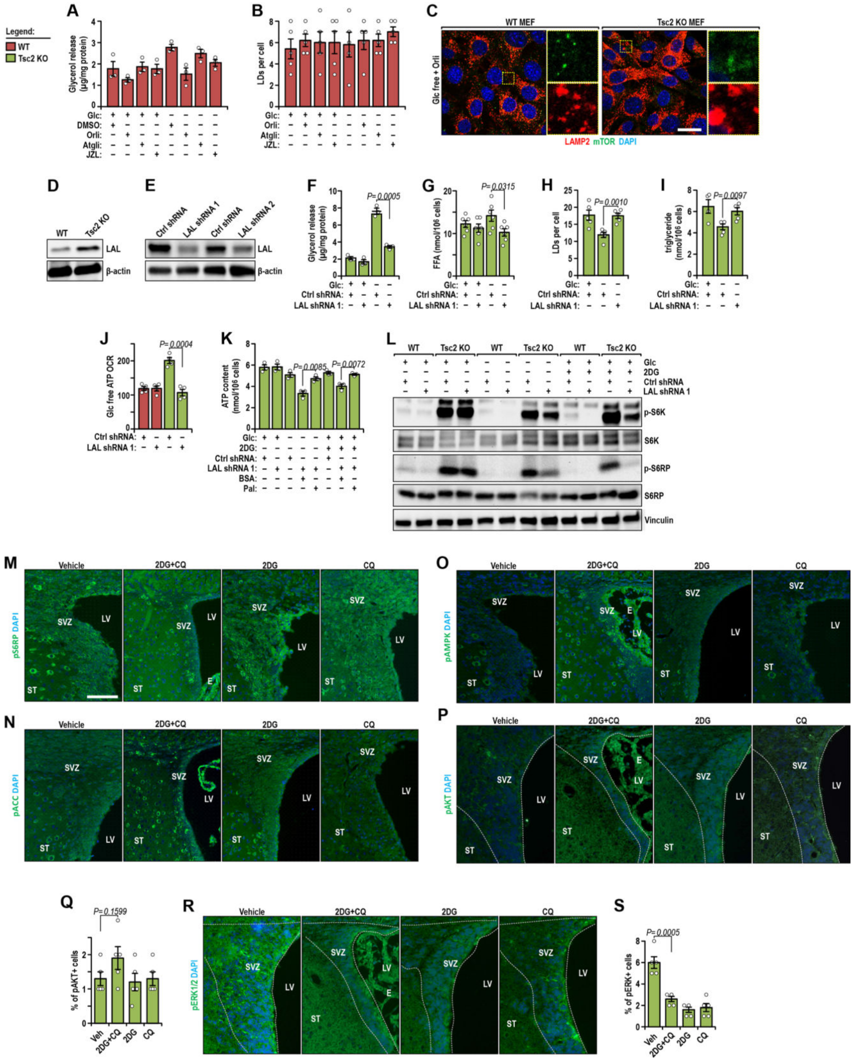

Extended Data Fig. 7. Lipophagy released FFAs in energy stressed mTORC1 hyperactivated Tsc-deficient cells.

(A, B) Mean ± SE of glycerol release from (A) and the number of LDs in (B) WT MEF under normal media and glucose-free media (without FBS) for 2 hours supplemented with DMSO, orlistat, Atglistat, or JZL were shown. n = 3 (A) and 5 (B) independent experiments.

(C) Immunofluorescence of LAMP2, mTOR, and DAPI in Orlistat treated WT and Tsc2 KO MEF under glucose-free media (without FBS) for 2 hours. Insets in details on right panels. Three independent experiments gave similar results.

(D) Lysates from WT and Tsc2 KO MEF were examined by immunoblot of LAL and actin. Three independent experiments gave similar results.

(E) Lysates from scrambled shRNA and two individual LAL shRNAs infected WT MEF were examined by immunoblot of LAL and actin. Three independent experiments gave similar results.

(F and G) Mean ± SE of the glycerol release (F) and FFA content (G) from scrambled shRNA and LAL shRNA #1 infected WT and Tsc2 KO MEF in normal media and glucose-free media for 2 hours were shown. n = 3 (F) and 6 (G) independent experiments.

(H and I) Mean ± SE of the number of LDs (H) and the content of triglyceride (I) in scrambled shRNA and LAL shRNA #1 infected Tsc2 KO MEF under normal media and glucose deprivation conditions. n = 5 independent experiments.

(J) Mean ± SE of ATP related OCR of scrambled shRNA and LAL shRNA #1 infected WT and Tsc2 KO MEF under glucose deprivation conditions. n = 4 independent experiments.

(K) Mean ± SE of the ATP content of scrambled shRNA and LAL shRNA #1 infected Tsc2 KO MEF in normal media, glucose-free media and 2DG media with or without supplement of BSA-Palmitate for 2 hours were shown. n = 3 independent experiments.

(L) Lysates from scrambled shRNA and LAL shRNA #1 infected WT and Tsc2 KO MEF in normal media, glucose-free media, and 2DG supplemented media for 2 hours. The levels of phosphorylated S6K, total S6K, phosphorylated S6RP, total S6RP, and vinculin were examined by Western blot as indicated. Three independent experiments gave similar results.

(M-O) Immunofluorescence of pS6RP (M), pACC (N), pAMPK (O) and DAPI in SVZ of *Tsc1*^{GFAP} cKO mice treated with vehicle, 2DG, CQ, and CQ^{+}2DG. Five independent experiments gave similar results.

(P) Immunofluorescence of pAKT and DAPI in SVZ of *Tsc1*^{GFAP} cKO mice treated with vehicle, 2DG, CQ, and CQ^{+}2DG. Five independent experiments gave similar results.

(Q) Mean ± SE of the percentage of pAKT^{+} cells in SVZ of *Tsc1*^{GFAP} cKO mice treated with vehicle, 2DG, CQ, and CQ^{+}2DG. n = 5 independent experiments.

(R) Immunofluorescence of pERK and DAPI in SVZ of *Tsc1*^{GFAP} cKO mice treated with vehicle, 2DG, CQ, and CQ^{+}2DG. Five independent experiments gave similar results.

(S) Mean ± SE of the percentage of pERK^{+} cells in SVZ of *Tsc1*^{GFAP} cKO mice treated with vehicle, 2DG, CQ, and CQ^{+}2DG. n = 5 independent experiments.

Dotted lines indicated the boundaries between SVZ and LV. E: ependymal layer; LV: lateral ventricle; ST: striatum; SVZ: subventricular zone.

Bar = 10 μm (C); Bar = 100μm (M-P, R). Data were analyzed by two-tailed Student’s t test (A, B, F-K), one-way ANOVA with Tukey’s post-hoc test (Q, S).

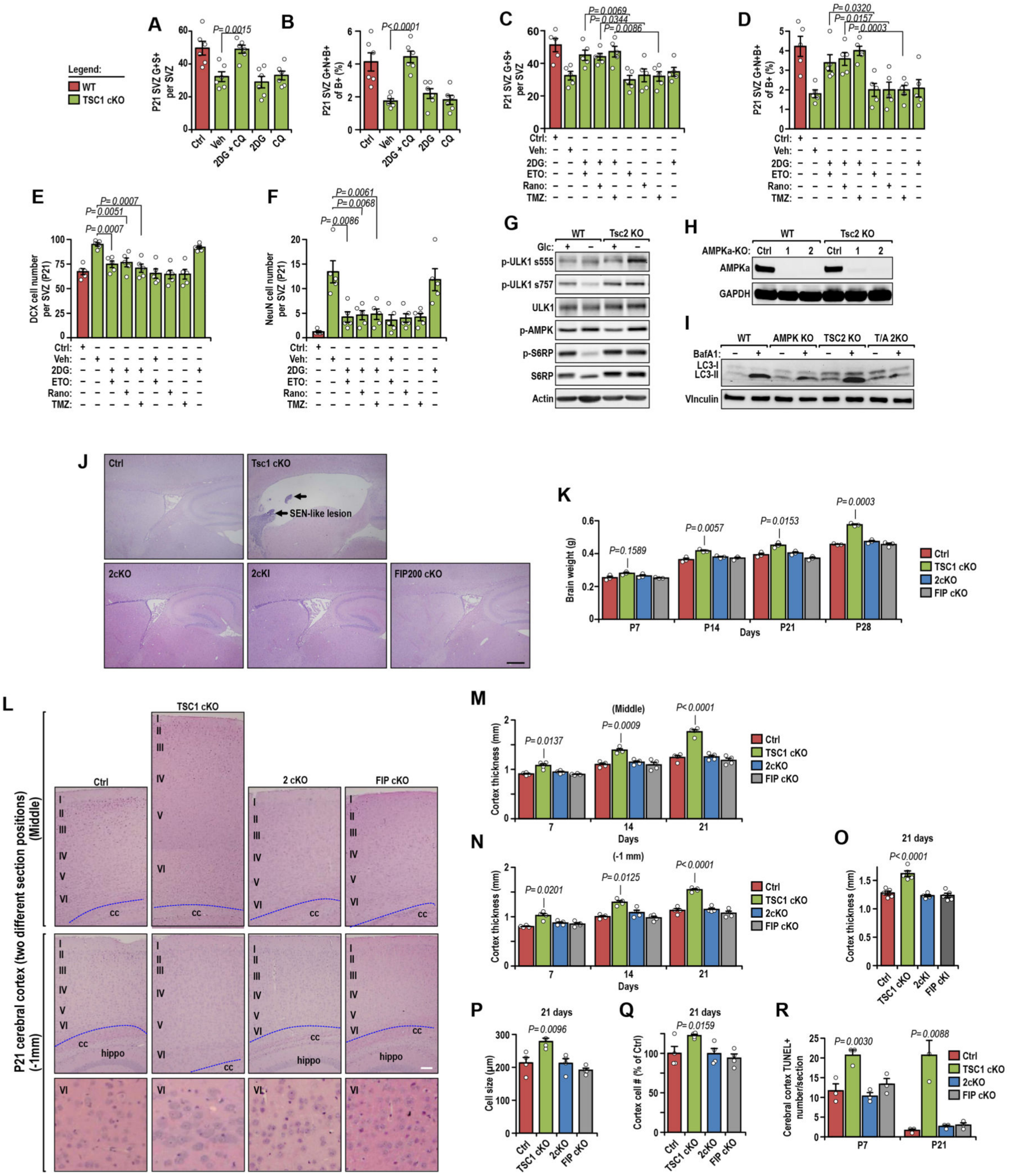

Extended Data Fig. 8. AMPK activation stimulated autophagy and lipophagy was required in Tsc-deficient cells. Postnatal developmental defects of cerebral cortex in *$Tsc1^{GFAP}$*cKO mice were rescued in 2cKO mice.

(A) Mean ± SE of the number of GFAP$^+$Sox2$^+$ NSC in SVZof Ctrl mice treated with CQ$^+$2DG and *$Tsc1^{GFAP}$* cKO mice treated with vehicle, 2DG, CQ, and CQ$^+$2DG. n = 6 independent experiments.

(B) Mean ± SE of the number of GFAP$^+$Nestin$^+$BrdU$^+$ cell of total BrdU$^+$ cells (B) in SVZ of Ctrl mice treated with CQ$^+$2DG and *$Tsc1^{GFAP}$* cKO mice treated with vehicle, 2DG, CQ, and CQ$^+$2DG. n = 6 independent experiments.

(C) Mean ± SE of the number of GFAP$^+$Sox2$^+$ NSC in SVZof *Tsc1^{GFAP}* cKO mice treated with vehicle, 2DG, ETO, Rano, TMZ, ETO$^+$2DG, Rano$^+$2DG, and TMZ$^+$2DG are shown. n = 5 independent experiments.

(D) Mean ± SE of the number of GFAP$^+$Nestin$^+$BrdU$^+$ cells of total BrdU$^+$ cells in SVZ of Ctrl and *Tsc1^{GFAP}* cKO mice treated with vehicle, 2DG, ETO, Rano, TMZ, ETO$^+$2DG, Rano$^+$2DG, and TMZ$^+$2DG. n = 5 independent experiments.

(E and F) Mean ± SE of the number of DCX$^+$ cells (E) and NeuN$^+$ cells (F) in SVZ of Ctrl and *Tsc1^{GFAP}* cKO mice treated with vehicle, 2DG, ETO, Rano, TMZ, ETO$^+$2DG, Rano $^+$2DG, and TMZ$^+$2DG. n = 5 independent experiments.

(G) Lysates from WT and Tsc2 KO MEF in normal or glucose-free media were examined by immunoblots with antibodies as indicated. Three independent experiments gave similar results.

(H) Lysates from WT MEF, AMPKα1 KO MEF (2 independent clones), Tsc2 KO MEF, and 2KO MEF (2 independent clones) were examined by immunoblots with antibodies, as indicated. Three independent experiments gave similar results.

(I) Lysates were extracted from WT MEF, AMPKα1 KO MEF, Tsc2 KO MEF, and 2KO MEF in glucose-free media with or without BafA1 for 2 hours. The levels of LC3-II and vinculin were examined. Three independent experiments gave similar results.

(J) H&E staining of sagittal sectioned brain indicating hydrocephaly of *Tsc1^{GFAP}* cKO lateral ventricle, but not in Ctrl, 2cKO, 2cKI, and *FIP200^{GFAP}* cKO mice at P21. Arrows indicated SEN-like structures in *Tsc1^{GFAP}* cKO brain. Three independent experiments gave similar results.

(K) Mean ± SE of brain weight of Ctrl, *Tsc1^{GFAP}* cKO, 2cKO, and *FIP200^{GFAP}* cKO mice at P7, P14, and P21. n = 3 independent experiments.

(L) H&E staining of sagittal sectioned brain indicating thicker cortex of *Tsc1^{GFAP}* cKO brain, but not in Ctrl, 2cKO, 2cKI, and *FIP200^{GFAP}* cKO mice at P21. The sagittal sections for middle of the brain (middle position) and 1 mm lateral to the middle position were stained. The dashed lines indicated the boundaries of cortex and CC. Four independent experiments gave similar results.

(M-O) Mean ± SE of cortex thickness of Ctrl, *Tsc1^{GFAP}* cKO, 2cKO, and *FIP200^{GFAP}* cKO mice at two different section positions (M and N) at P7, P14, and P21, and P21 2cKI (O) mice at middle position. n = 4 (M and N) and 5 (O) independent experiments.

(P-R) Mean ± SE of cortex cell size (P) and cortex cell number (Q) of Ctrl, *Tsc1^{GFAP}* cKO, 2cKO, and *FIP200^{GFAP}* cKO mice by H&E staining at P21, and cortex TUNEL-positive cell number (R) at P7 and P21. n = 4 (P and Q) and 3 (R) independent experiments.

CC: corpus callosum; hippo: hippocampus; I-VI indicates layers of cerebral cortex. Bar = 50 μm. Data were analyzed by one-way ANOVA with Tukey’s post-hoc test (A-F, O-R), one-way ANOVA (K, M, N, R).

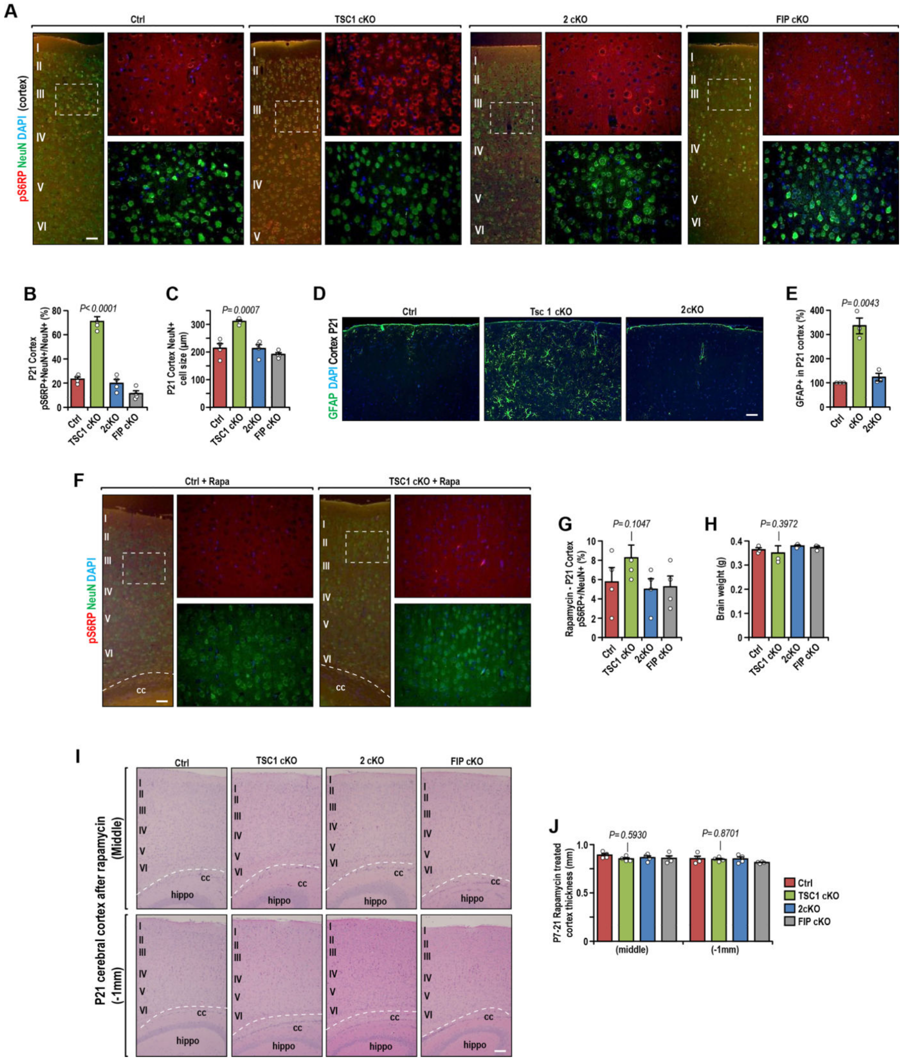

Extended Data Fig. 9. Postnatal developmental defects of cerebral cortex in *Tsc1*^{GFAP}cKO mice were rescued in 2cKO mice and by Rapamycin treatment.

(A) Immunofluorescence of pS6RP, NeuN, and DAPI in cortex of Ctrl, *Tsc1*^{GFAP} cKO, 2cKO, and *FIP200*^{GFAP} cKO mice at P21. Inset shows details of pS6RP and NeuN in boxed area. Four independent experiments gave similar results.

(B, C) Mean ± SE of the percentage of pS6RP^{+}NeuN^{+} of NeuN^{+} cells (B) and the cell size of NeuN^{+} cells (C) in the cortex of Ctrl, *Tsc1*^{GFAP} cKO, 2cKO, and *FIP200*^{GFAP} cKO mice at P21. n = 4 independent experiments for at least 300 cells counted.

(D) Immunofluorescence of GFAP and DAPI in SVZ of Ctrl, *Tsc1*^{GFAP} cKO, 2cKO, and *FIP200*^{GFAP} cKO mice at P21. Four independent experiments gave similar results.

(E) Mean ± SE of the relative percentage of GFAP^{+} cells in the cortex of Ctrl, *Tsc1*^{GFAP} cKO, and 2cKO mice at P21. n = 4 independent experiments for at least 300 cells counted.

(F) Immunofluorescence of pS6RP, NeuN, and DAPI in the cortex of rapamycin treated Ctrl and *Tsc1*^{GFAP} mice at P21. Inset shows details of pS6RP and NeuN in boxed area. The dashed lines indicated the boundaries of cortex and CC. Four independent experiments gave similar results.

(G) Mean ± SE of the percentage of pS6RP$^+$NeuN$^+$ of NeuN$^+$ cells in the cortex of rapamycin treated Ctrl and *Tsc1*^{GFAP} cKO mice at P21. n = 4 independent experiments for at least 300 cells counted.

(H) Mean ± SE of the brain weight of rapamycin treated Ctrl and *Tsc1*^{GFAP} cKO mice at P21. n = 3 independent experiments.

(I) H&E staining of sagittal sectioned brain indicating cortex of Ctrl, *Tsc1*^{GFAP} cKO, 2cKO, 2cKI, and *FIP200*^{GFAP} cKO mice at P21. The sagittal sections for middle of the brain (middle position) and 1 mm lateral to the middle position were stained. The dashed lines indicated the boundaries of cortex and CC. Four independent experiments gave similar results.

(J) Mean ± SE of cortex thickness of Ctrl, *Tsc1*^{GFAP} cKO, 2cKO, and *FIP200*^{GFAP} cKO mice at two different section positions at P21. n = 3 (middle) or 4 (-1mm) independent experiments.

CC: corpus callosum; hippo: hippocampus; I-VI indicates layers of cerebral cortex. Bar = 50 μm. Data were analyzed by one-way ANOVA with Tukey's post-hoc test (B, C, E, S, H, J).

Supplementary Material

Refer to Web version on PubMed Central for supplementary material.

Acknowledgements

We thank our colleagues Drs. Y. Zheng, Q. Lu, M. Czyzyk-Krzeska, D. Hui and, T. Cunningham; our laboratory members; G. Doerman, and Dr. B. Peace. Research was supported by NIH grants NS094144 and CA211066 to JLG and NS103981 to CW.

References

1. Saxton RA & Sabatini DM mTOR Signaling in Growth, Metabolism, and Disease. Cell 169, 361–371 (2017).
2. Hay N. & Sonenberg N. Upstream and downstream of mTOR. Genes Dev 18, 1926–1945 (2004). [PubMed: 15314020]
3. Ben-Sahra I. & Manning BD mTORC1 signaling and the metabolic control of cell growth. Curr Opin Cell Biol 45, 72–82 (2017). [PubMed: 28411448]
4. Costa-Mattioli M. & Monteggia LM mTOR complexes in neurodevelopmental and neuropsychiatric disorders. Nature neuroscience 16, 1537–1543 (2013). [PubMed: 24165680]
5. Crino PB mTOR: A pathogenic signaling pathway in developmental brain malformations. Trends in molecular medicine 17, 734–742 (2011). [PubMed: 21890410]
6. Chan JA et al. Pathogenesis of tuberous sclerosis subependymal giant cell astrocytomas: biallelic inactivation of TSC1 or TSC2 leads to mTOR activation. Journal of neuropathology and experimental neurology 63, 1236–1242 (2004). [PubMed: 15624760]
7. Magri L. et al. Sustained Activation of mTOR Pathway in Embryonic Neural Stem Cells Leads to Development of Tuberous Sclerosis Complex-Associated Lesions. Cell Stem Cell 9, 447–462 (2011). [PubMed: 22056141]
8. Way SW et al. Loss of Tsc2 in radial glia models the brain pathology of tuberous sclerosis complex in the mouse. Hum Mol Genet 18, 1252–1265 (2009). [PubMed: 19150975]
9. Zhou J. et al. Tsc1 mutant neural stem/progenitor cells exhibit migration deficits and give rise to subependymal lesions in the lateral ventricle. Genes Dev 25, 1595–1600 (2011). [PubMed: 21828270]
10. Zordan P. et al. Tuberous sclerosis complex-associated CNS abnormalities depend on hyperactivation of mTORC1 and Akt. J Clin Invest 128, 1688–1706 (2018). [PubMed: 29389670]

11. Knobloch M. et al. Metabolic control of adult neural stem cell activity by Fasn-dependent lipogenesis. Nature 493, 226–230 (2013). [PubMed: 23201681]
12. Rafalski VA & Brunet A. Energy metabolism in adult neural stem cell fate. Progress in neurobiology 93, 182–203 (2011). [PubMed: 21056618]
13. Shyh-Chang N, Daley GQ & Cantley LC Stem cell metabolism in tissue development and aging. Development 140, 2535–2547 (2013). [PubMed: 23715547]
14. Stoll EA et al. Neural Stem Cells in the Adult Subventricular Zone Oxidize Fatty Acids to Produce Energy and Support Neurogenic Activity. Stem cells 33, 2306–2319 (2015). [PubMed: 25919237]
15. Xie Z, Jones A, Deeney JT, Hur SK & Bankaitis VA Inborn Errors of Long-Chain Fatty Acid beta-Oxidation Link Neural Stem Cell Self-Renewal to Autism. Cell reports 14, 991–999 (2016). [PubMed: 26832401]
16. Duvel K. et al. Activation of a metabolic gene regulatory network downstream of mTOR complex 1. Mol Cell 39, 171–183 (2010). [PubMed: 20670887]
17. Hu CJ, Wang LY, Chodosh LA, Keith B. & Simon MC Differential roles of hypoxia-inducible factor 1alpha (HIF-1alpha) and HIF-2alpha in hypoxic gene regulation. Molecular and cellular biology 23, 9361–9374 (2003). [PubMed: 14645546]
18. Porstmann T. et al. SREBP activity is regulated by mTORC1 and contributes to Akt-dependent cell growth. Cell metabolism 8, 224–236 (2008). [PubMed: 18762023]
19. Laplante M. & Sabatini DM An emerging role of mTOR in lipid biosynthesis. Current biology : CB 19, R1046–1052 (2009).
20. Valvezan AJ et al. mTORC1 Couples Nucleotide Synthesis to Nucleotide Demand Resulting in a Targetable Metabolic Vulnerability. Cancer Cell 32, 624–638 e625 (2017). [PubMed: 29056426]
21. Levine B. & Kroemer G. Autophagy in the pathogenesis of disease. Cell 132, 27–42 (2008). [PubMed: 18191218]
22. Mizushima N, Levine B, Cuervo AM & Klionsky DJ Autophagy fights disease through cellular self-digestion. Nature 451, 1069–1075 (2008). [PubMed: 18305538]
23. Mizushima N. & Komatsu M. Autophagy: renovation of cells and tissues. Cell 147, 728–741 (2011). [PubMed: 22078875]
24. Ng S, Wu YT, Chen B, Zhou J. & Shen HM Impaired autophagy due to constitutive mTOR activation sensitizes TSC2-null cells to cell death under stress. Autophagy 7, 1173–1186 (2011). [PubMed: 21808151]
25. Chen Y, Wei H, Liu F. & Guan JL Hyperactivation of mammalian target of rapamycin complex 1 (mTORC1) promotes breast cancer progression through enhancing glucose starvation-induced autophagy and Akt signaling. J Biol Chem 289, 1164–1173 (2014). [PubMed: 24275666]
26. Di Nardo A. et al. Neuronal Tsc1/2 complex controls autophagy through AMPK-dependent regulation of ULK1. Hum Mol Genet 23, 3865–3874 (2014). [PubMed: 24599401]
27. Parkhitko A. et al. Tumorigenesis in tuberous sclerosis complex is autophagy and p62/sequestosome 1 (SQSTM1)-dependent. Proceedings of the National Academy of Sciences of the United States of America 108, 12455–12460 (2011). [PubMed: 21746920]
28. Lamark T. & Johansen T. Aggrephagy: selective disposal of protein aggregates by macroautophagy. International journal of cell biology 2012, 736905 (2012).
29. Kim I, Rodriguez-Enriquez S. & Lemasters JJ Selective degradation of mitochondria by mitophagy. Archives of biochemistry and biophysics 462, 245–253 (2007). [PubMed: 17475204]
30. Kubli DA & Gustafsson AB Mitochondria and mitophagy: the yin and yang of cell death control. Circulation research 111, 1208–1221 (2012). [PubMed: 23065344]
31. Palikaras K. & Tavernarakis N. Mitophagy in neurodegeneration and aging. Frontiers in genetics 3, 297 (2012). [PubMed: 23267366]
32. Singh R. et al. Autophagy regulates lipid metabolism. Nature 458, 1131–1135 (2009). [PubMed: 19339967]
33. Liu K. & Czaja MJ Regulation of lipid stores and metabolism by lipophagy. Cell Death Differ 20, 3–11 (2013). [PubMed: 22595754]

34. Martinez-Lopez N. et al. Autophagy in the CNS and Periphery Coordinate Lipophagy and Lipolysis in the Brown Adipose Tissue and Liver. Cell metabolism 23, 113–127 (2016). [PubMed: 26698918]
35. Hara T. et al. Suppression of basal autophagy in neural cells causes neurodegenerative disease in mice. Nature 441, 885–889 (2006). [PubMed: 16625204]
36. Komatsu M. et al. Loss of autophagy in the central nervous system causes neurodegeneration in mice. Nature 441, 880–884 (2006). [PubMed: 16625205]
37. Wang C. et al. Elevated p62/SQSTM1 determines the fate of autophagy-deficient neural stem cells by increasing superoxide. The Journal of cell biology 212, 545–560 (2016). [PubMed: 26929451]
38. Wang C, Liang CC, Bian ZC, Zhu Y. & Guan JL FIP200 is required for maintenance and differentiation of postnatal neural stem cells. Nat Neurosci 16, 532–542 (2013). [PubMed: 23542691]
39. Kim J, Kundu M, Viollet B. & Guan KL AMPK and mTOR regulate autophagy through direct phosphorylation of Ulk1. Nat Cell Biol 13, 132–141 (2011). [PubMed: 21258367]
40. Kwiatkowski DJ et al. A mouse model of TSC1 reveals sex-dependent lethality from liver hemangiomas, and up-regulation of p70S6 kinase activity in Tsc1 null cells. Human molecular genetics 11, 525–534 (2002). [PubMed: 11875047]
41. Sun S. et al. Constitutive Activation of mTORC1 in Endothelial Cells Leads to the Development and Progression of Lymphangiosarcoma through VEGF Autocrine Signaling. Cancer cell 28, 758–772 (2015). [PubMed: 26777415]
42. Wang C, Yeo S, Haas MA & Guan JL Autophagy gene FIP200 in neural progenitors non-cell autonomously controls differentiation by regulating microglia. The Journal of cell biology 216, 2581–2596 (2017). [PubMed: 28634261]
43. Sharma M. et al. Subependymal giant cell astrocytoma: a clinicopathological study of 23 cases with special emphasis on proliferative markers and expression of p53 and retinoblastoma gene proteins. Pathology 36, 139–144 (2004). [PubMed: 15203749]
44. Chen S. et al. Distinct roles of autophagy-dependent and -independent functions of FIP200 revealed by generation and analysis of a mutant knock-in mouse model. Genes Dev 30, 856–869 (2016). [PubMed: 27013233]
45. Liu J. et al. Beclin1 controls the levels of p53 by regulating the deubiquitination activity of USP10 and USP13. Cell 147, 223–234 (2011). [PubMed: 21962518]
46. Sancak Y. et al. Ragulator-Rag complex targets mTORC1 to the lysosomal surface and is necessary for its activation by amino acids. Cell 141, 290–303 (2010). [PubMed: 20381137]
47. Nigrovic LE, Kimia AA, Shah SS & Neuman MI Relationship between cerebrospinal fluid glucose and serum glucose. N Engl J Med 366, 576–578 (2012). [PubMed: 22316468]
48. Kimmelman AC & White E. Autophagy and Tumor Metabolism. Cell Metab 25, 1037–1043 (2017). [PubMed: 28467923]
49. Galluzzi L, Pietrocola F, Levine B. & Kroemer G. Metabolic control of autophagy. Cell 159, 1263–1276 (2014). [PubMed: 25480292]
50. Son J. et al. Glutamine supports pancreatic cancer growth through a KRAS-regulated metabolic pathway. Nature 496, 101–105 (2013). [PubMed: 23535601]
51. Chakrabarti P, English T, Shi J, Smas CM & Kandror KV Mammalian target of rapamycin complex 1 suppresses lipolysis, stimulates lipogenesis, and promotes fat storage. Diabetes 59, 775–781 (2010). [PubMed: 20068142]
52. Tuunanen H. et al. Trimetazidine, a metabolic modulator, has cardiac and extracardiac benefits in idiopathic dilated cardiomyopathy. Circulation 118, 1250–1258 (2008). [PubMed: 18765391]
53. Zacharowski K, Blackburn B. & Thiemermann C. Ranolazine, a partial fatty acid oxidation inhibitor, reduces myocardial infarct size and cardiac troponin T release in the rat. European journal of pharmacology 418, 105–110 (2001). [PubMed: 11334871]
54. Huang SC et al. Cell-intrinsic lysosomal lipolysis is essential for alternative activation of macrophages. Nat Immunol 15, 846–855 (2014). [PubMed: 25086775]
55. Mayer N. et al. Development of small-molecule inhibitors targeting adipose triglyceride lipase. Nat Chem Biol 9, 785–787 (2013). [PubMed: 24096302]

56. Long JZ et al. Selective blockade of 2-arachidonoylglycerol hydrolysis produces cannabinoid behavioral effects. Nat Chem Biol 5, 37–44 (2009). [PubMed: 19029917]
57. Ouimet M. et al. Autophagy regulates cholesterol efflux from macrophage foam cells via lysosomal acid lipase. Cell Metab 13, 655–667 (2011). [PubMed: 21641547]
58. Dubland JA & Francis GA Lysosomal acid lipase: at the crossroads of normal and atherogenic cholesterol metabolism. Frontiers in cell and developmental biology 3, 3 (2015). [PubMed: 25699256]
59. Zhang Y. et al. Coordinated regulation of protein synthesis and degradation by mTORC1. Nature 513, 440–443 (2014). [PubMed: 25043031]
60. Schmidt EV The role of c-myc in cellular growth control. Oncogene 18, 2988–2996 (1999). [PubMed: 10378694]
61. Morita M. et al. mTORC1 controls mitochondrial activity and biogenesis through 4E-BP-dependent translational regulation. Cell Metab 18, 698–711 (2013). [PubMed: 24206664]
62. Wei H. et al. Suppression of autophagy by FIP200 deletion inhibits mammary tumorigenesis. Genes Dev 25, 1510–1527 (2011). [PubMed: 21764854]
63. Yang S. et al. Pancreatic cancers require autophagy for tumor growth. Genes Dev 25, 717–729 (2011). [PubMed: 21406549]
64. Guo JY et al. Activated Ras requires autophagy to maintain oxidative metabolism and tumorigenesis. Genes Dev 25, 460–470 (2011). [PubMed: 21317241]
65. Nie D. et al. Tsc2-Rheb signaling regulates EphA-mediated axon guidance. Nat Neurosci 13, 163–172 (2010). [PubMed: 20062052]
66. Yeo SK, Wen J, Chen S. & Guan JL Autophagy Differentially Regulates Distinct Breast Cancer Stem-like Cells in Murine Models via EGFR/Stat3 and Tgfbeta/Smad Signaling. Cancer Res 76, 3397–3410 (2016). [PubMed: 27197172]

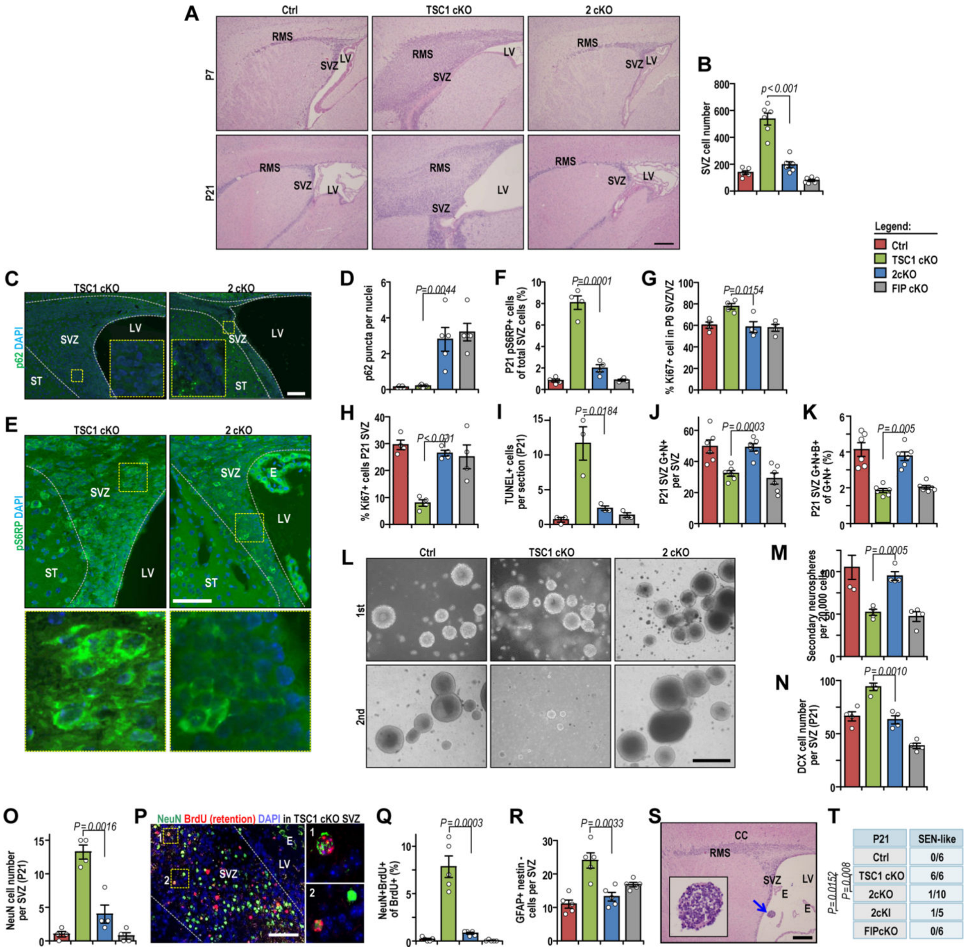

P21	SEN-like
Ctrl	0/6
TSC1 cKO	6/6
2cKO	1/10
2cKI	1/5
FIPcKO	0/6

Figure 1. Inactivating FIP200 rescued defective postnatal NSCs in *Tsc1*^{GFAP} cKO mice.

(A) H&E staining of P7 and P21SVZ and RMS from Ctrl, *Tsc1*^{GFAP} cKO, and 2cKO mice.

(B) Mean ± SE of P21SVZ cell number of Ctrl, *Tsc1*^{GFAP} cKO, 2cKO, and *FIP200*^{GFAP} cKO mice. n = 6 animals.

(C) Immunofluorescence of p62 and DAPI in P21SVZ of *Tsc1*^{GFAP} cKO, and 2cKO mice. Inset: p62 aggregates.

(D) Mean ± SE of p62 puncta in P21 SVZ of Ctrl, *Tsc1*^{GFAP} cKO, 2cKO, and *FIP200*^{GFAP} cKO mice. n = 5 animals.

(E) Immunofluorescence of pS6RP and DAPI in P21SVZ of *Tsc1*^{GFAP} cKO and 2cKO mice. Bottom panels: boxed area

(F) Mean ± SE of pS6RP$^+$cells in P21SVZ of Ctrl, *Tsc1*^{GFAP} cKO, 2cKO, and *FIP200*^{GFAP} cKO mice. n = 4 animals.

(G, H) Mean ± SE of Ki67$^+$cell percentage in P0 (G) and P21 (H) SVZ from Ctrl, *Tsc1*^{GFAP} cKO, 2cKO, and *FIP200*^{GFAP} cKO mice. n = 4 animals.

(I) Mean ± SE of TUNEL$^+$ cells in P21SVZ and RMS of Ctrl, *Tsc1*^{GFAP} cKO, 2cKO, and *FIP200*^{GFAP} cKO mice. n = 3 animals.

(J, K) Mean ± SE of GFAP$^+$Nestin$^+$ NSC (J) and GFAP$^+$Nestin$^+$BrdU$^+$ cells (K) vs total GFAP$^+$Nestin$^+$ cells in P21SVZ of Ctrl, *Tsc1*^{GFAP} cKO, 2cKO, and *FIP200*^{GFAP} cKO mice. n = 6 animals.

(L) Phase contrast images of primary (upper) and secondary (lower) neurospheres from P21SVZ cells of Ctrl, *Tsc1*^{GFAP} cKO, and 2cKO mice. Four independent experiments gave similar results.

(M) Mean ± SE of secondary neurospheres from P21SVZ cells of Ctrl, *Tsc1*^{GFAP} cKO, 2cKO, and *FIP200*^{GFAP} cKO mice. n = 4 animals.

(N, O) Mean ± SE of DCX^{+} (N) and NeuN^{+} (O) cells in P21SVZ of Ctrl, *Tsc1*^{GFAP} cKO, 2cKO, and *FIP200*^{GFAP} cKO are shown. n = 4 animals.

(P) Immunofluorescence of NeuN, BrdU, and DAPI in *Tsc1*^{GFAP} cKO P21SVZ. BrdU labeled at P7 was retained for 14 days to trace NeuN^{+} cells. Boxed detail: cell #1 and #2. Five independent experiments gave similar results.

(Q) Mean ± SE of the percentage of BrdU+NeuN+ cells vs total BrdU+ cells in Ctrl, Tsc1GFAP cKO, 2cKO, and FIP200GFAP cKO SVZ. n = 5 animals.

(R) Mean ± SE of GFAP+nestin-cells in P21SVZ of Ctrl, Tsc1GFAP cKO, 2cKO, and FIP200GFAP cKO mice. n = 5 animals.

(S) H&E staining of SEN-like lesion (arrow) in *Tsc1*^{GFAP} cKO P21brain. Inset: detail of “floating” lesion. Five independent experiments gave similar results.

(T) Frequency of SEN-like lesions in Ctrl, *Tsc1*^{GFAP} cKO, 2cKO, 2cKI, and *FIP200*^{GFAP} cKO P21mice. Animal number is in the table.

Dotted lines (C, E, P) indicate the SVZ boundaries. CC: corpus callosum; E: ependymal; LV: lateral ventricle; RMS: rostral migratory stream; SEN-like: subependymal nodule-like lesion; SVZ: subventricular zone. Bar = 100 μm. Data were analyzed by one-way ANOVA with Tukey’s post-hoc test (B, D, F-K, M-O, Q and R), Chi-Square test (T).

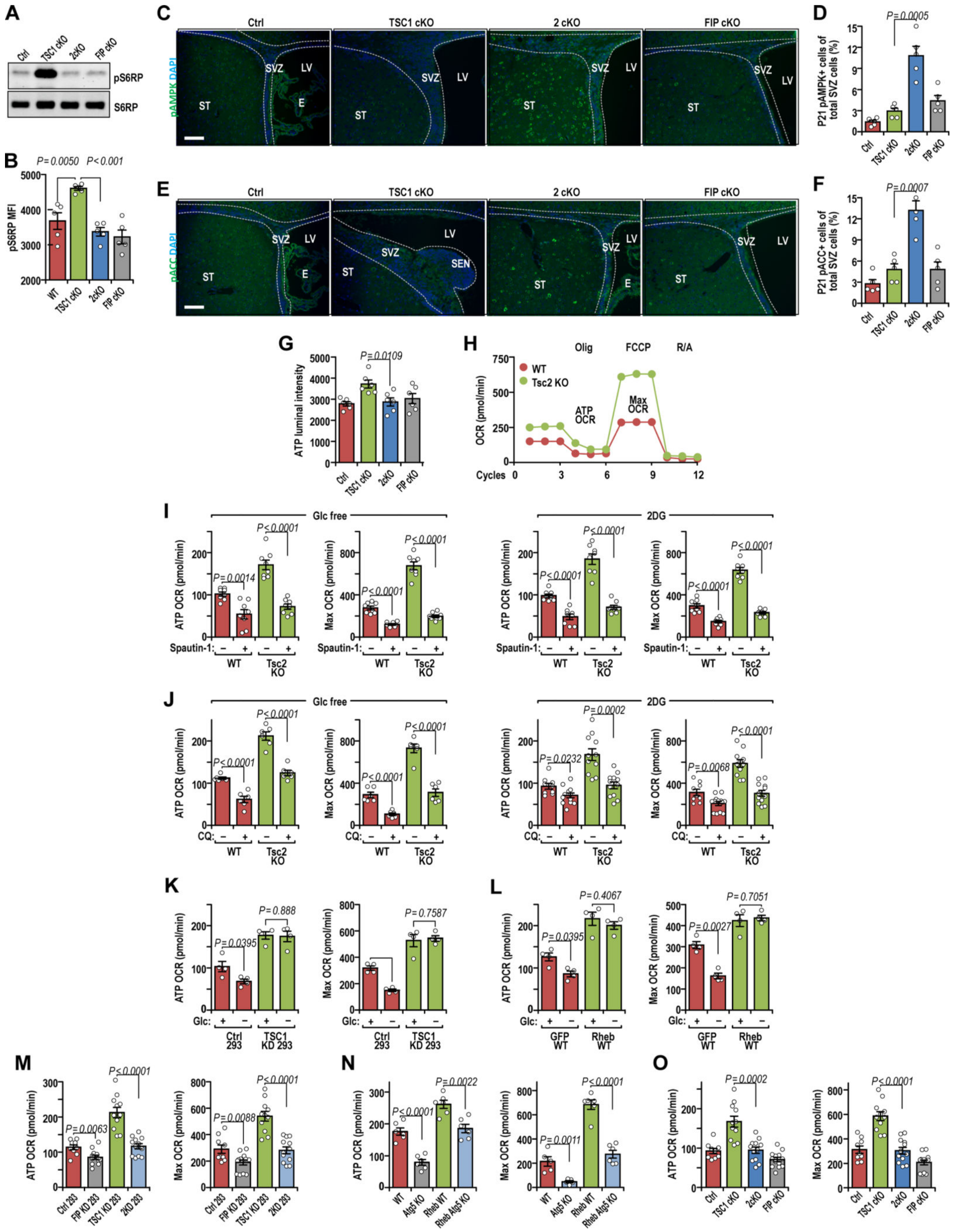

Figure 2. Autophagy supplies ATP to sustain hyperactivation of mTORC1 in Tsc-deficient cells under energy stress.

(A) Lysates from Ctrl, *Tsc1*^{GFAP} cKO, 2cKO, and *FIP200*^{GFAP} cKO neurospheres in glucose-free media for 2 hrs probed for phosphorylated and total S6RP. Three independent experiments gave similar results.

(B) Mean ± SE of mean fluorescent intensity (MFI) of pS6RP from dissociated Ctrl, *Tsc1*^{GFAP} cKO, 2cKO, and *FIP200*^{GFAP} cKO neurospheres in glucose-free media for 2 hrs. n = 5 animals.

(C) Immunofluorescence of pAMPK and DAPI in P21SVZ of Ctrl, *Tsc1*^{GFAP} cKO, 2cKO, and *FIP200*^{GFAP} cKO mice.

(D) Mean ± SE of percentage of pAMPK^{+} cells in P21SVZ of Ctrl, *Tsc1*^{GFAP} cKO, 2cKO, and *FIP200*^{GFAP} cKO mice. n = 5 animals.

(E) Immunofluorescence of pACC and DAPI in P21SVZ of Ctrl, *Tsc1*^{GFAP} cKO, 2cKO, and *FIP200*^{GFAP} cKO mice.

(F) Mean ± SE of percentage of pACC^{+} cells in P21SVZ SVZ of Ctrl, *Tsc1*^{GFAP} cKO, 2cKO, and *FIP200*^{GFAP} cKO mice. n = 5 animals.

(G) Mean ± SE of ATP content of isolated primary neurospheres from Ctrl, *Tsc1*^{GFAP} cKO, 2cKO, and *FIP200*^{GFAP} cKO mice. n = 6 animals.

(H) Measurement of OCR in WT and Tsc2 KO MEF under normal conditions. Olig: oligomycin, FCCP: trifluoromethoxy carbonylcyanide phenylhydrazone, R/A: rotenone and antimycin.

(I and J) Mean ± SE of ATP related and maximum OCR of 10 μM Spautin1 (I) and 20 μM CQ (J) treated WT and Tsc2 KO MEF under glucose-free or 2DG treatment. n = 6 independent experiments.

(K) Mean ± SE of ATP related and maximum OCR in Ctrl and TSC1 KD 293 cells under normal and glucose-free conditions. n = 4 independent experiments.

(L) Mean ± SE of ATP related and maximum OCR in GFP and Rheb-CA overexpressing MEF under normal and glucose-free conditions. n = 4 independent experiments.

(M) Mean ± SE of ATP related and maximum OCR in Ctrl, FIP200 KD, TSC1 KD, and 2KD 293 cells under glucose-free conditions. n = 9–12 independent experiments.

(N) Mean ± SE of ATP related and maximum OCR in WT, Atg5 KO, Rheb-CA overexpressing, and Rheb-CA overexpressing Atg5 KO MEF under glucose-free conditions. n = 5–6 independent experiments.

(O) Mean ± SE of ATP related and maximum OCR in isolated primary neurospheres from Ctrl, *Tsc1*^{GFAP} cKO, 2cKO, and *FIP200*^{GFAP} cKO mice under glucose-free conditions. n = 5 animals. Data were analyzed by one-way ANOVA with Tukey's post-hoc test (B, D, F, G, O), and two-tailed Student's t test (I-N).

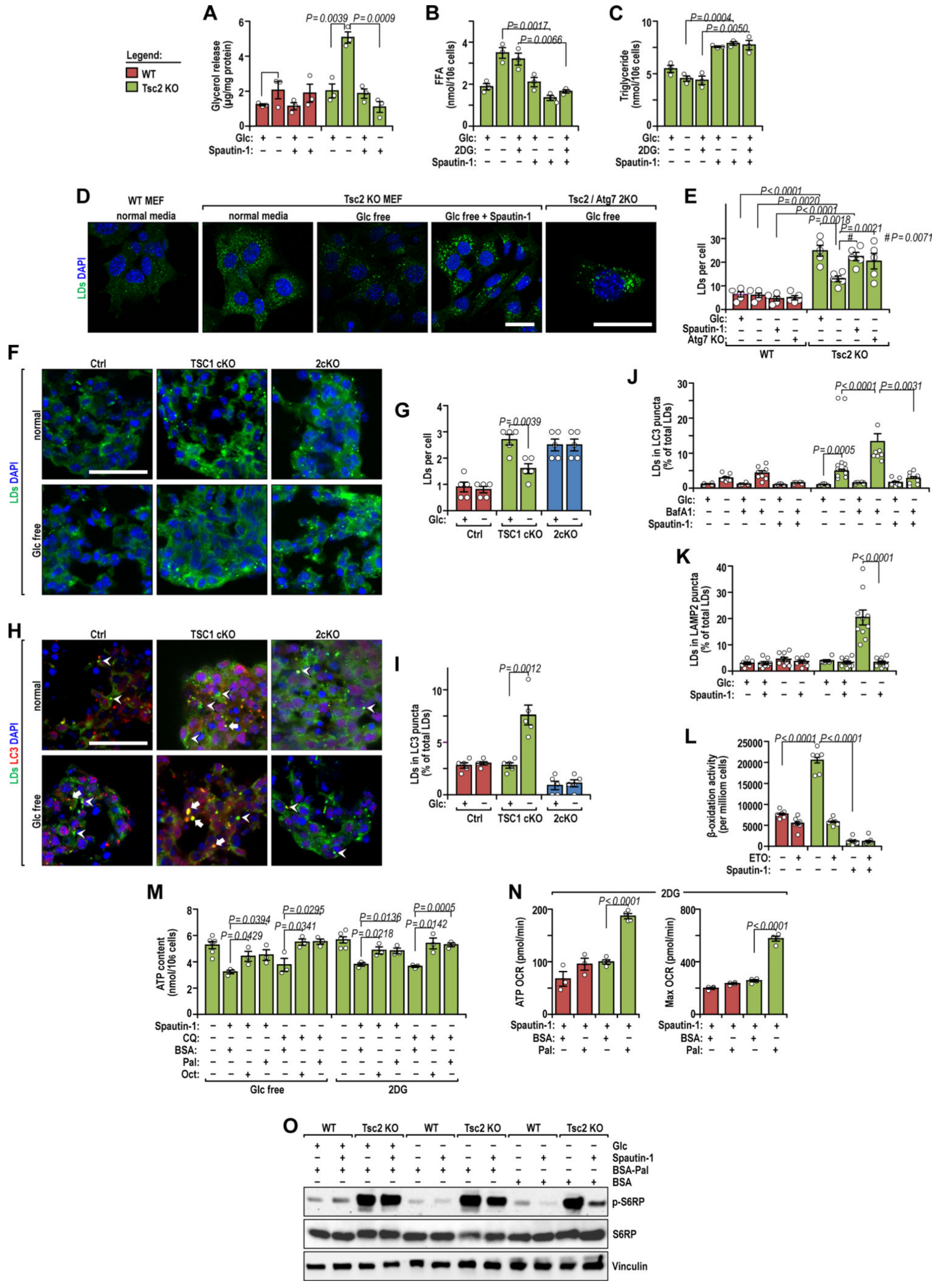

Figure 3. Autophagy degraded lipid storage of LDs in energy stressed Tsc-deficient cells.

(A) Mean ± SE of glycerol release from DMSO or Spautin1 treated WT and Tsc2 KO MEF in FBS-free normal and glucose-free media for 2 hrs. Spautin1 was pre-incubated for 12 hrs. n = 3 independent experiments.

(B, C) Mean ± SE of FFAs (B) and triglyceride (C) content of DMSO or Spautin1 treated Tsc2 KO MEF in FBS-free normal, glucose-free, and 2DG media for 2 hrs. n = 3 independent experiments.

(D) Fluorescence for lipid droplets and DAPI in WT, DMSO or Spautin1 treated Tsc2 KO and Tsc2/Atg7 2KO MEF under FBS-free normal or glucose-free conditions for 2 hrs.

(E) Mean ± SE of LDs of DMSO or Spautin1 treated WT, Tsc2 KO, and Tsc2/Atg7 2KO MEF in FBS-free normal and glucose-free media for 2 hrs. n = 5 independent experiments.

(F) Fluorescence for lipid droplets and DAPI in isolated primary neurospheres from Ctrl, $Tsc1^{GFAP}$ cKO, and 2cKO mice under FBS-free normal and glucose-free media for 2 hr.

(G) Mean ± SE of LDs in isolated primary neurospheric cells from Ctrl, Tsc1GFAP cKO, and 2cKO mice under FBS-free normal and glucose-free media for 2 hrs. n = 5 independent experiments.

(H) Immunofluorescence for lipid droplets, LC3 and DAPI in isolated primary neurospheres from Ctrl, Tsc1GFAP cKO, and 2cKO mice under FBS-free normal or glucose-free media for 2 hrs. Arrows: LDs/LC3 double positive; arrowheads: LD3 alone.

(I) Mean ± SE of percentage of LDs on $LC3^+$ puncta of isolated primary neurospheres from Ctrl, Tsc1GFAP cKO, and 2cKO mice in FBS-free normal and glucose-free media for 2 hrs. n = 5 independent experiments.

(J) Mean ± SE of the percentage of LDs on $LC3^+$ puncta of DMSO, BafA1 (100 nM), Spautin1 treated WT MEF and Tsc2 KO MEF in FBS-free normal and glucose-free media for 2 hrs. n = 4–9 independent experiments.

(K) Mean ± SE of the percentage of LDs on $LAMP2^+$ lysosome of DMSO or Spautin1 treated WT MEF and Tsc2 KO MEF in FBS-free normal and glucose-free media for 2 hrs. n = 6–10 independent experiments.

(L) Mean ± SE of the β-oxidation activity of DMSO or Spautin1 treated WT MEF and Tsc2 KO MEF in FBS-free glucose-free media for 2 hrs. Etomoxir (ETO) inhibited β-oxidation. n = 6 independent experiments.

(M) Mean ± SE of ATP in Spautin1-treated Tsc2 KO MEF, re-supplemented with BSA or 1 mM BSA-FFAs in FBS-free glucose-free, and 2DG media for 2 hrs are shown. BSA-FFAs were pre-incubated for 2 hrs. n = 3–6 independent experiments.

(N) Mean ± SE of ATP related and maximum OCR of Spautin1 treated WT and Tsc2 KO MEF re-supplemented with BSA or 1 mM BSA-Palmitate and 2DG. n = 3–4 independent experiments.

(O) Lysates from DMSO and Spautin1 treated WT and Tsc2 KO MEF in normal and glucose-free media for 2 hrs probed by immunoblot. BSA or BSA-palmitate were pre-incubated for 2 hrs. Three independent experiments gave similar results.

Bar = 10 μm for D and 5 μm for F and H. Data were analyzed by two-tailed Student's t test (A-C, M, N), one-way ANOVA with Tukey's post-hoc test (E, G, I-L).

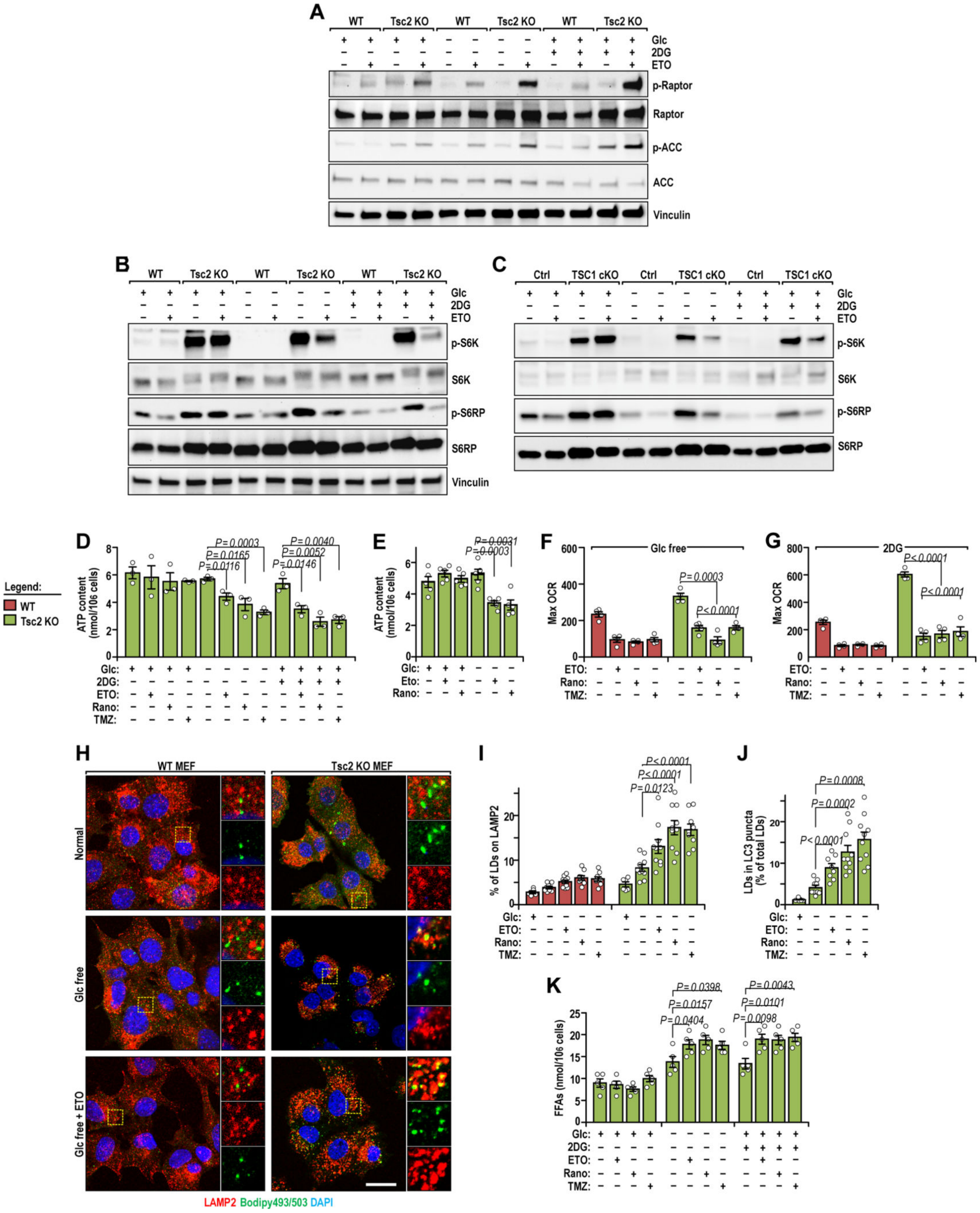

Figure 4. β-oxidation of FFAs to sustain hyperactivation of mTORC1 in energy stressed Tsc-deficient cells.

(A and B) Lysates from WT and Tsc2 KO MEF in FBS-free normal, glucose-free, and 2DG media for 2 hrs. ETO was pre-incubated for 12 hrs followed by 2 hrs energy stress. (A) Phosphorylated and total Raptor, phosphorylated and total ACC, and vinculin. (B) Phosphorylated and total S6K, phosphorylated and S6RP, and vinculin.

(C) Lysates from Ctrl and Tsc1 cKO neurosphere in FBS-free normal, glucose-free, and 2DG media for 2 hrs. ETO was pre-incubated for 12 hrs and followed by 2 hrs energy stress.

Phosphorylated and total S6K, phosphorylated and total S6RP are shown. Three independent experiments gave similar results. (A-C).
(D) Mean ± SE of ATP content of Tsc2 KO MEF treated with ETO (200 μM), TMZ (1 mM), and Rano (200 μM) in FBS-free normal, glucose-free, and 2DG media for 2 hrs. Inhibitors were pre-incubated for 12 hrs. n = 3 independent experiments.
(E) Mean ± SE of ATP of $Tsc1^{GFAP}$ cKO primary neurospheres treated with ETO (200 μM) or Rano (200 μM) in normal or glucose-free media. Inhibitors were pre-incubated for 12 hrs. n = 5 independent experiments.
(F and G) Mean ± SE of maximum OCR of ETO, TMZ, and Rano treated WT and Tsc2 KO MEF under glucose-free (F) or 2DG treatment (G). n = 4 independent experiments.
(H) Immunofluorescence of LDs, LAMP2 and DAPI in ETO treated WT and Tsc2 KO MEF under FBS-free normal and glucose-free media for 2 hrs. Insets in details on right panels.
(I and J) Mean ± SE of percentage of LDs on $LAMP2^+$ structure (I) and on $LC3^+$ puncta (J) of ETO, TMZ, and Rano treated Tsc2 KO MEF in FBS-free normal and glucose-free media for 2 hrs. n = 5–10 (I) and 10 (J) independent experiments.
(K) Mean ± SE of FFA content of ETO, TMZ, and Rano treated Tsc2 KO MEF in FBS-free normal, glucose-free, and 2DG media for 2 hrs. n = 5 independent experiments.
Bar = 10 μm. Data were analyzed by two-tailed Student's t test, (D-G, I-K).

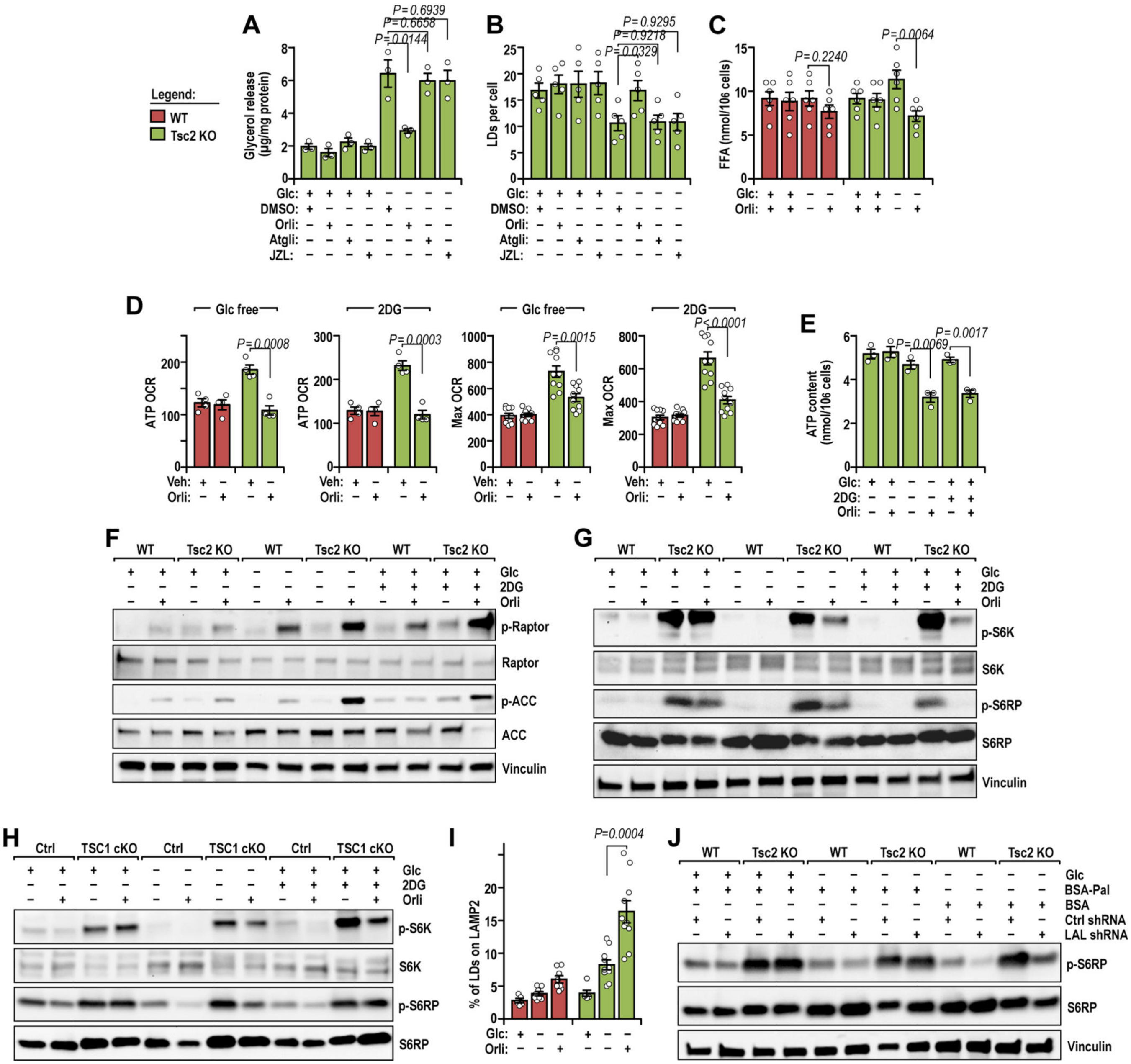

Figure 5. LAL release FFAs from LDs to sustain hyperactivation of mTORC1 in Tsc-deficient cells.

(A-C) Mean ± SE of glycerol release (A), lipid droplet number (B) and FFAs content (C) from DMSO, Atgli, JZL (A and B) and 6200 μM Orlistat (A-C) treated WT and Tsc2 KO MEF in FBS-free normal and glucose-free media for 2 hrs. Atgli, JZL and Orlistat were pre-incubated for 24 hrs. n = 3 (A), 5 (B), 6 (C) independent experiments.

(D) Mean ± SE of ATP related and maximum OCR of vehicle or Orlistat treated WT and Tsc2 KO MEF under glucose-free or 2DG treatment. n = 4–10 independent experiments.

(E) Mean ± SE of ATP content of Orlistat treated WT and Tsc2 KO MEF in FBS-free normal, glucose–free, and 2DG media for 2 hrs. n = 3 independent experiments.

(F and G) Lysates from DMSO or Orlistat treated WT and Tsc2 KO MEF in FBS-free normal, glucose–free, and 2DG media for 2 hrs examined by immunoblot. Orlistat was pre-incubated for 24 hrs. (F) Phosphorylated and total Raptor, phosphorylated and total ACC, and vinculin. (G) Phosphorylated and total S6K, phosphorylated and total S6RP, and vinculin.

(H) Lysates from Ctrl and Tsc1 cKO neurospheres in FBS-free normal, glucose–free, and 2DG media for 2 hrs. Orlistat was pre-incubated for 24 hrs followed by 2 hrs energy stress. Phosphorylated and total S6K, phosphorylated and total S6RP are shown. Three independent experiments gave similar results (F-H).

(I) Mean ± SE of percentage of LDs on LAMP2$^+$ structure of Orlistat treated WT and Tsc2 KO MEF in FBS-free normal and glucose-free media for 2 hrs. n = 5–10 independent experiments.

(J) Lysates from scrambled and LAL shRNA #1 infected WT and Tsc2 KO MEF in normal and glucose-free media for 2 hrs. BSA or BSA-palmitate were pre-incubated for 2 hr. Phosphorylated and total S6RP and vinculin were examined by immunoblot. Three independent experiments gave similar results.

Data were analyzed by teo-tailed Student’s t test (A-E, I).

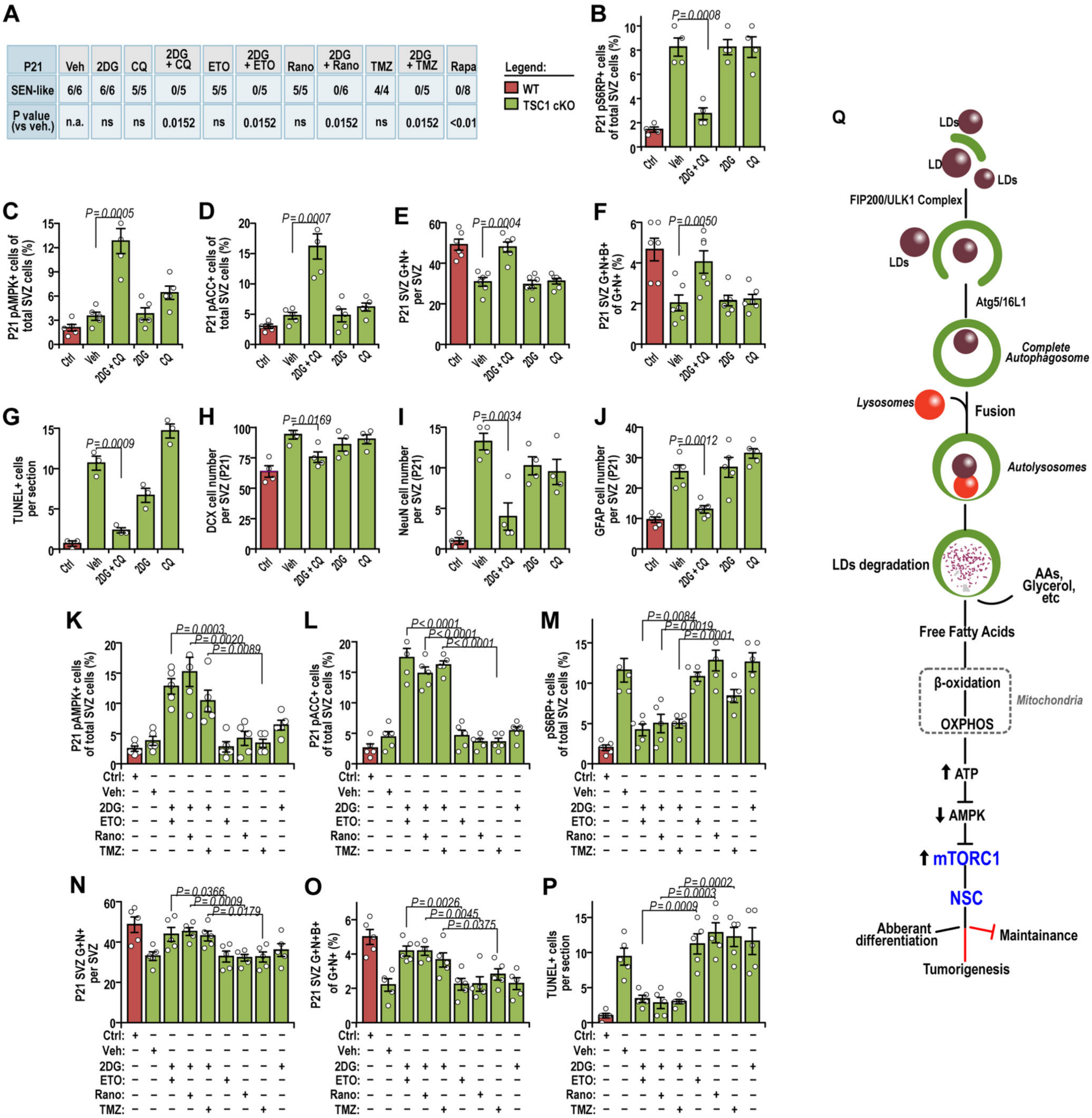

P21	Veh	2DG	CQ	2DG + CQ	ETO	2DG + ETO	Rano	2DG + Rano	TMZ	2DG + TMZ	Rapa
SEN-like	6/6	6/6	5/5	0/5	5/5	0/5	5/5	0/6	4/4	0/5	0/8
P value (vs veh.)	n.a.	ns	ns	0.0152	ns	0.0152	ns	0.0152	ns	0.0152	<0.01

Figure 6. Targeting lipophagy to rescue defects in postnatal Tsc1-deficient NSC.

(A) SEN-like lesion in *Tsc1*^{GFAP} cKO treated with vehicle, 2DG, CQ, etomoxir, ranolazine, trimetazidine, CQ+2DG, etomoxir+2DG, ranolazine+2DG, trimetazidine+2DG. Positive control: rapamycin. Animal number is indicated in the figure.

(B-D) Mean ± SE of percentage of pS6RP^{+} (B), pAMPK+ (C), and pACC+ cells (D) in SVZ of CQ+2DG treated Ctrl, and vehicle, 2DG, CQ, and CQ+2DG treated *Tsc1*^{GFAP} cKO mice. n = 4 (B) and 5 (C, D) independent experiments.

(E) Mean ± SE of GFAP$^+$Nestin$^+$ NSC in SVZ of CQ+2DG treated Ctrl, and vehicle, 2DG, CQ, and CQ+2DG treated *Tsc1^{GFAP}* cKO mice. n = 6 independent experiments.

(F) Mean ± SE of GFAP$^+$Nestin$^+$ BrdU$^+$ cells of total GFAP$^+$Nestin$^+$ cells in SVZ of CQ +2DG treated Ctrl, and vehicle, 2DG, CQ, and CQ+2DG treated *Tsc1^{GFAP}* cKO mice. n = 6 independent experiments.

(G) Mean ± SE of TUNEL$^+$ cells in SVZ of CQ+2DG treated Ctrl, and vehicle, 2DG, CQ, and CQ+2DG treated *Tsc1^{GFAP}* cKO mice. n = 3 independent experiments.

(H-J) Mean ± S.E. of the percentage of DCX$^+$ cells (H), NeuN$^+$ cells (I), and GFAP$^+$nestin$^-$ cells (J) from CQ+2DG treated Ctrl, and vehicle, 2DG, CQ, and CQ+2DG treated *Tsc1^{GFAP}* cKO mice. n = 4 (H and I) and 5 (J) independent experiments.

(K-M) Mean ± SE of percentage of pAMPK+ (K), pACC+ (L), and pS6RP$^+$cells (M) in SVZ of vehicle, 2DG, ETO, Rano, TMZ, ETO+2DG, Rano+2DG, and TMZ+2DG treated Ctrl and *Tsc1^{GFAP}* cKO mice. n = 5 independent experiments.

(N) Mean ± SE of GFAP$^+$Nestin$^+$ NSC in SVZ with vehicle, 2DG, ETO, Rano, TMZ, ETO +2DG, Rano+2DG, and TMZ+2DG treated Ctrl and *Tsc1^{GFAP}* cKO mice. n = 5 independent experiments.

(O) Mean ± SE of GFAP$^+$Nestin$^+$BrdU$^+$ cells of total GFAP$^+$Nestin$^+$ cells in SVZ of Ctrl and *Tsc1^{GFAP}* cKO mice treated with vehicle, 2DG, ETO, Rano, TMZ, ETO+2DG, Rano +2DG, and TMZ+2DG. n = 5 independent experiments.

(P) Mean ± SE of TUNEL$^+$ cells in SVZ of Ctrl and *Tsc1^{GFAP}* cKO mice treated with vehicle, 2DG, ETO, Rano, TMZ, ETO+2DG, Rano+2DG, and TMZ+2DG. n = 5 independent experiments.

(Q) Working model of sustained hyperactivated mTORC1 in TSC-deficient NSC.

Data were analyzed by Chi-Square test (A), one-way ANOVA with Tukey's post-hoc test (B-P).